



Universiteit
Leiden
The Netherlands

Spin-label EPR Approaches to Protein Interactions

Son, M. van

Citation

Son, M. van. (2014, December 4). *Spin-label EPR Approaches to Protein Interactions*. *Casimir PhD Series*. Retrieved from <https://hdl.handle.net/1887/29986>

Version: Not Applicable (or Unknown)

License: [Leiden University Non-exclusive license](#)

Downloaded from: <https://hdl.handle.net/1887/29986>

Note: To cite this publication please use the final published version (if applicable).

Cover Page



Universiteit Leiden



The handle <http://hdl.handle.net/1887/29986> holds various files of this Leiden University dissertation.

Author: Son, Martin van

Title: Spin-label EPR approaches to protein interactions

Issue Date: 2014-12-04

Spin-label EPR Approaches to Protein Interactions

Proefschrift

ter verkrijging van
de graad van Doctor aan de Universiteit Leiden,
op gezag van Rector Magnificus prof.mr. C.J.J.M. Stolker,
volgens besluit van het College voor Promoties
te verdedigen op donderdag 4 december 2014
klokke 11:15 uur

door

Martin van Son
geboren te Rotterdam
in 1982

PROMOTIECOMMISSIE

Promotor:	Prof. dr. E.J.J. Groenen	Universiteit Leiden
Copromotor:	Dr. M. Huber	Universiteit Leiden
Leden:	Dr. A. Schnegg	Helmholtz-Zentrum Berlin
	Dr. ir. C.P.M. van Mierlo	Universiteit Wageningen
	Prof. dr. E.R. Eliel	Universiteit Leiden
	Prof. dr. J.M. van Ruitenbeek	Universiteit Leiden
	Prof. dr. T. Schmidt	Universiteit Leiden
	Prof. dr. M. Ubbink	Universiteit Leiden

Cover design: Sven Hoek

Printed by CPI-Wöhrmann Print Service – Zutphen.

The work presented in this thesis was supported with financial aid by The Netherlands Organization for Scientific Research (NWO), grant 700.58.014.

Casimir PhD Series, Delft-Leiden, 2014-29

ISBN 978-90-8593-202-4

An electronic version of this thesis is available at
<https://openaccess.leidenuniv.nl>

CONTENTS

List of abbreviations	5	
Chapter 1	Introduction	7
	1.1 Spin labelling	8
	1.2 EPR principles	9
	1.3 Relaxation of electron spins	16
	1.4 Spin-spin interactions	18
	1.5 Scope of thesis	24
	References	25
Chapter 2	Heterodimer formation of membrane-fusion	
	E/K peptides studied by continuous-wave EPR ...	27
	2.1 Introduction	27
	2.2 Material and methods	31
	2.3 Results	35
	2.4 Discussion	38
	References	41
Chapter 3	The complex of cytochrome <i>c</i> with cytochrome <i>c</i>	
	peroxidase studied by spin-label, multi-frequency	
	electron paramagnetic resonance	43
	3.1 Introduction	43
	3.2 Material and methods	46
	3.3 Results	55
	3.4 Discussion	64
	References	67

Chapter 4	Spin-spin interaction in rigid 3_{10}-helical peptides with TOAC spin-labels: an EPR power-saturation study	69
	4.1 Introduction	69
	4.2 Material and methods	71
	4.3 Results	73
	4.4 Discussion	78
	4.5 Conclusions	82
	References	83
Chapter 5	Equilibrium unfolding of flavodoxin from double electron-electron resonance distance constraints	85
	5.1 Introduction	85
	5.2 Material and methods	87
	5.3 Results	90
	5.4 Discussion	98
	References	103
	Summary	105
	Samenvatting	109
	Curriculum vitae	113
	List of publications	115
	Acknowledgements	117

LIST OF ABBREVIATIONS

BSA	bovine serum albumin
cw	continuous wave
Cc, CcP	cytochrome <i>c</i> , cytochrome <i>c</i> peroxidase
DEER	double electron-electron resonance
DTT	dithiothreitol
EPR	electron paramagnetic resonance
fdx	flavodoxin
GuHCl	guanidine hydrochloride
id/od	inner diameter/outer diameter
KPP _i	potassium pyrophosphate
MTSL	<i>S</i> -(1-oxyl-2,2,5,5-tetramethyl-2,5-dihydro-1H-pyrrol-3-yl)- methyl methanesulfonylthioate
NMR	nuclear magnetic resonance
PCA	principal component analysis
PDB	Protein Data Bank
SL	spin label
TOAC	alpha-amino acid 2,2,6,6-tetramethylpiperidine-1-oxyl-4- amino-4-carboxylic acid
\vec{A}, a	hyperfine tensor, hyperfine-coupling constant
\vec{B}, B	magnetic-field vector, magnetic-field magnitude
B_1	microwave-magnetic-field magnitude
$E, \Delta E$	energy, difference in energy
η	viscosity
\vec{g}, g	<i>g</i> tensor, <i>g</i> value

\mathcal{H}	Hamiltonian
h	Planck's constant
\bar{I}	nuclear-spin angular-momentum operator
I	nuclear-spin quantum number
J	exchange coupling
k_B	Boltzmann constant
K_D	dissociation constant
μ_B	Bohr magneton
ν	frequency
\bar{S}	electron-spin-angular-momentum operator
S	electron-spin quantum number
T_1, T_2	longitudinal relaxation time, transverse relaxation time
τ_r	rotation-correlation time
Y	peak-to-peak amplitude
ω_{dd}	dipole-dipole coupling

ala	A	alanine
arg	R	arginine
cys	C	cysteine
glu	E	glutamic acid
gly	G	glycine
his	H	histidine
ile	I	isoleucine
lys	K	lysine
leu	L	leucine
tyr	Y	tyrosine
trp	W	tryptophan

1

INTRODUCTION

In 2014, the Protein Data Bank (PDB) reached the milestone of containing 100,000 biomolecular structures in its data base^[1]. The fundament for this affluence has been laid in the early 1950s, when the first structures of the α -helix and β -sheet^[2], the coiled-coil motif^[3], and DNA^[4,5] were reported. The large majority of the structures in the PDB were elucidated with X-ray crystallography, which even today remains the most common tool to determine biomolecular structure. This technique allows biomolecules to be studied at atomic detail, which has immensely enhanced our understanding of molecular biology.

X-ray crystallography provides only a static picture of the biomolecules, whose nature is essentially dynamic, and whose flexibility is closely related to their biological function. Think about the dynamics involved in processes such as protein folding, enzymatic reactions, or interacting proteins that facilitate membrane fusion and electron transfer. Methods other than X-ray crystallography are needed to study the dynamics of these biomolecules, to obtain information that goes beyond the static picture.

Electron paramagnetic resonance (EPR) spectroscopy^[6] is well suited for providing such information and is sufficiently sensitive to characterize large biomolecular complexes. Distances of a few nanometres, corresponding to the

typical size of biomacromolecules, are accessible and EPR is able to deal with complex structures and high molecular weights. Furthermore, the application does not require that the molecules of interest are crystallized, which for many biomolecules and complexes is not feasible.

To use EPR, the biomolecule of interest must contain an unpaired electron – a requirement that is not met by all molecules. A paramagnetic centre, however, can be introduced by a nitroxide spin label.

1.1 Spin labelling

The spin-labelling technique^[7-9] allows a spin label to be introduced at a particular position in the biomolecule. Figure 1.1 shows the chemical structure of the two spin labels used in this work: *S*-(1-oxyl-2,2,5,5-tetramethyl-2,5-dihydro-1H-pyrrol-3-yl)methyl methanesulfonylthioate (MTSL)^[10] and the alpha-amino acid 2,2,6,6-tetramethyl-piperidine-1-oxyl-4-amino-4-carboxylic acid (TOAC)^[11].

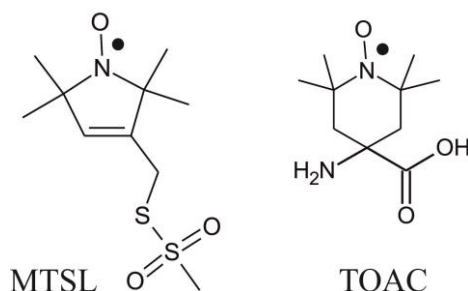


Figure 1.1 The chemical structures of the spin labels *S*-(1-oxyl-2,2,5,5-tetramethyl-2,5-dihydro-1H-pyrrol-3-yl) methyl methanesulfonylthioate (MTSL), and alpha-amino acid 2,2,6,6-tetramethyl-piperidine-1-oxyl-4-amino-4-carboxylic acid (TOAC). Both spin labels have an unpaired electron (indicated by a dot) located at the N–O bond.

Owing to its convenience and chemical stability, the MTSL label has become the most widely used spin label for characterizing nanosecond motions^[12], for determining distances^[13], and for mapping protein topology^[14]. The five-membered nitroxide ring is covalently coupled via the disulphide bond to a cysteine. A great advantage is gained when combined with mutagenesis. This allows a cysteine to be introduced at a selected position in a peptide or protein, thereby giving numerous possibilities to introduce the MTSL label into the biomolecule. This technique, known as site-directed spin labelling (SDSL)^[15], has become a powerful tool for probing structure and dynamics of both water-soluble and membrane proteins of arbitrary molecular weight^[14]. The five bonds that connect the ring of MTSL to the protein backbone are somewhat of a disadvantage, because they introduce additional degrees of motional freedom. Consequently, translating interspin-distance measurements and spatial-orientation information into structural constraints is challenging.

The TOAC label is an unnatural amino acid, which can be incorporated into peptides during synthesis. The six-membered nitroxide ring is rigid and directly fused to the peptide backbone. Hence, the nanosecond motions detected with EPR can be directly related to the peptide mobility. Unlike MTSL, the TOAC label cannot be easily incorporated into selected sites of proteins.

1.2 EPR principles

The spin of an unpaired electron has two, degenerate states. When an external magnetic field \bar{B} is applied, the energy levels for these states are split due to the interaction of the spin with the field. This is called the Zeeman interaction, named after the Nobel laureate Pieter Zeeman. In 1896, he discovered the effect

of a strong magnetic field on the electromagnetic spectrum emitted by sodium^[16].

We shall consider an electron spin, which interacts with a magnetic field, and has a hyperfine coupling (hf) with one neighbouring nuclear spin. Then, the spin Hamiltonian is

$$\mathcal{H} = \mathcal{H}_Z + \mathcal{H}_{hf} = \mu_B \bar{\mathbf{B}} \cdot \bar{\mathbf{g}} \cdot \bar{\mathbf{S}} + \bar{\mathbf{S}} \cdot \bar{\mathbf{A}} \cdot \bar{\mathbf{I}}, \quad (1.1)$$

where μ_B is the Bohr magneton, $\bar{\mathbf{g}}$ is the g tensor, $\bar{\mathbf{S}}$ is the electron spin angular momentum operator, $\bar{\mathbf{A}}$ is the hyperfine tensor, and $\bar{\mathbf{I}}$ is the nuclear spin angular momentum operator. The tensors $\bar{\mathbf{g}}$ and $\bar{\mathbf{A}}$ are diagonal in the principal-axes system. The principal axes coincide with the molecular axes of the spin label as defined in Figure 1.2. For a nitroxide spin label, typical tensors are $\bar{\mathbf{g}} = (g_{xx}, g_{yy}, g_{zz}) = (2.0088, 2.0061, 2.0027)$ and $\bar{\mathbf{A}} = (A_{xx}, A_{yy}, A_{zz}) = (16, 15, 104)$ MHz.

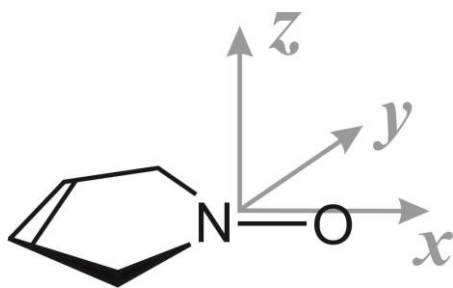


Figure 1.2 The molecular axes of the spin label MTSL. Only the ring structure including the nitroxide is shown. The x -axis coincides with the N—O bond, the z -axis is perpendicular to the ring.

To elaborate on the spin Hamiltonian in equation 1.1, two time regimes are distinguished: fast and slow molecular tumbling. Molecular tumbling is quantified in terms of the rotation-correlation time τ_r , which is the time a

molecule takes to rotate over one radian. Whether molecular tumbling is *fast* or *slow* depends on the value of τ_r with respect to the time scale of the EPR experiment.

Solution spectra – fast molecular tumbling

In the regime of fast tumbling, the molecular reorientations average out the anisotropic terms in equation 1.1. With

$$g = \frac{1}{3} \text{Tr } \bar{\bar{g}} \quad \text{and} \quad a = \frac{1}{3} \text{Tr } \bar{\bar{A}}, \quad (1.2)$$

the spin Hamiltonian has the isotropic form

$$\mathcal{H}_0 = g\mu_B \bar{\mathbf{B}} \cdot \bar{\mathbf{S}} + a\bar{\mathbf{S}} \cdot \bar{\mathbf{I}}. \quad (1.3)$$

Let the magnetic field have magnitude B and be directed along the molecular z -axis defined by the g tensor. Omitting the non-secular terms, equation 1.3 becomes

$$\mathcal{H}_0 = g\mu_B B S_z + a S_z I_z, \quad (1.4)$$

where S_z and I_z are the z -components of $\bar{\mathbf{S}}$ and $\bar{\mathbf{I}}$, respectively. The corresponding energy levels of the electron spin are

$$E(m_s, m_i) = g\mu_B B m_s + a m_s m_i, \quad (1.5)$$

where m_s is the eigenvalue of S_z (for the electron spin: $m_s = \pm\frac{1}{2}$) and m_i is the eigenvalue of I_z . A transition between the states occurs through absorption of microwaves whose frequency matches the energy difference. Satisfying the selection rules $\Delta m_s = \pm 1$ and $\Delta m_i = 0$, the resonance condition is met when

$$h\nu = g\mu_B B_0 + am_i, \quad (1.6)$$

where h is Planck's constant and ν is the frequency of the microwaves. The nitroxide spin labels used in this work (Figure 1.1), have the electron spin coupled to the nuclear spin of ^{14}N , for which $I = 1$, with the corresponding eigenvalues $m_i = -1, 0, +1$. For the electron spin of a nitroxide, a schematic energy diagram is shown in Figure 1.3, with the allowed EPR transitions indicated by grey arrows.

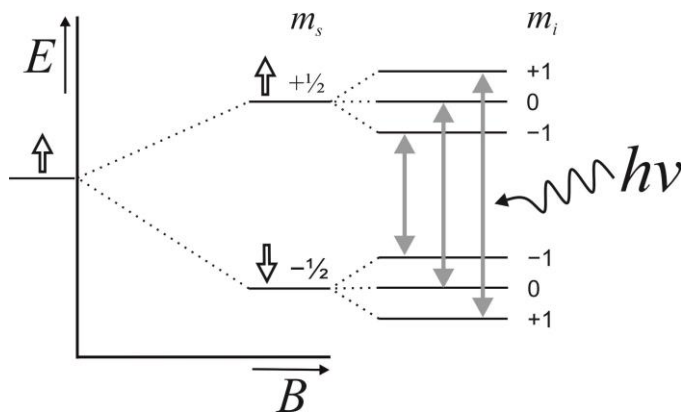


Figure 1.3 Schematic energy diagram of an electron spin ($S = \frac{1}{2}$) interacting with an external magnetic field and with a ^{14}N nuclear spin ($I = 1$). The grey arrows indicate the transitions between the magnetic sublevels, which are induced by microwaves ($h\nu$), satisfying the selection rules $\Delta m_s = \pm 1$ and $\Delta m_i = 0$.

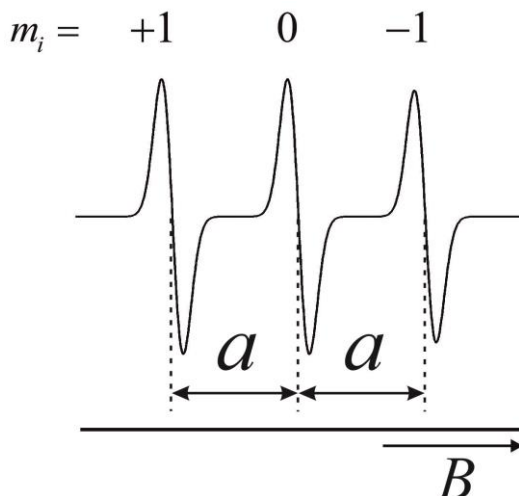


Figure 1.4 An example of a three-line EPR spectrum, which is typical for a nitroxide measured in cw mode. The lines are assigned to $m_i = +1, 0, -1$, and are spaced by the isotropic hyperfine coupling constant a .

Figure 1.4 shows an example of a three-line EPR spectrum, which is typical for a fast tumbling nitroxide measured in continuous wave (cw). The lines are designated with $m_i = +1, 0$, and -1 , corresponding to the ^{14}N nuclear spin states, which split the electron spin states into three sublevels. As indicated in Figure 1.4, the isotropic hyperfine coupling a can be determined directly from the EPR spectrum.

Solution spectra – slow molecular tumbling

The spin Hamiltonian in equation 1.1 can be considered as the sum of two parts: the isotropic \mathcal{H}_0 (given in equation 1.3) and a purely anisotropic \mathcal{H}_1 , which can be written as

$$\mathcal{H}_1 = \mu_B \vec{\mathbf{B}} \cdot \vec{\mathbf{g}}' \cdot \vec{\mathbf{S}} + \vec{\mathbf{S}} \cdot \vec{\mathbf{A}}' \cdot \vec{\mathbf{I}}. \quad (1.7)$$

Here, $\vec{\mathbf{g}}'$ and $\vec{\mathbf{A}}'$ are traceless tensors. In solution, the molecular motions make \mathcal{H}_1 a random function of time. In spite of the vanishing average value of \mathcal{H}_1 , broadening of the lines is expected to occur. The variations in linewidths and field positions, observed in solution spectra, derive from the fluctuations of the anisotropic terms of \mathcal{H}_1 by molecular motions.

The decisive effect of slow molecular tumbling on solution spectra is illustrated in Figure 1.5. Here, twelve simulated spectra show the rich variety in width and position of lines one would observe for different values of τ_r . The spectra were simulated at 9.8 GHz, 94 GHz, and 275 GHz, which are the experimental EPR frequencies available at Leiden Institute of Physics. In these simulations we assume τ_r to be isotropic, i.e., $\tau_{xx} = \tau_{yy} = \tau_{zz}$. The isotropic τ_r -values were set to 0.2 ns, 1 ns, 3 ns, and 10 ns at each of the microwave frequencies. Such simulations show that the anisotropy of $\vec{\mathbf{g}}$ becomes more apparent towards higher frequencies. Figure 1.6 shows that simulations at 94 GHz are also sensitive to the anisotropy in τ_r .

Software programs are available that enable the quantification of τ_r by fitting and/or simulating the cw-EPR spectrum. For example, Multicomponent^[17] uses the stochastic Liouville approach based on the program of Freed et al.^[18] for nitroxides in the slow-motion regime. The program EasySpin^[19] is more elaborate than Multicomponent, for it calculates the spin Hamiltonian for a broader range of paramagnetic species and in different motional regimes.

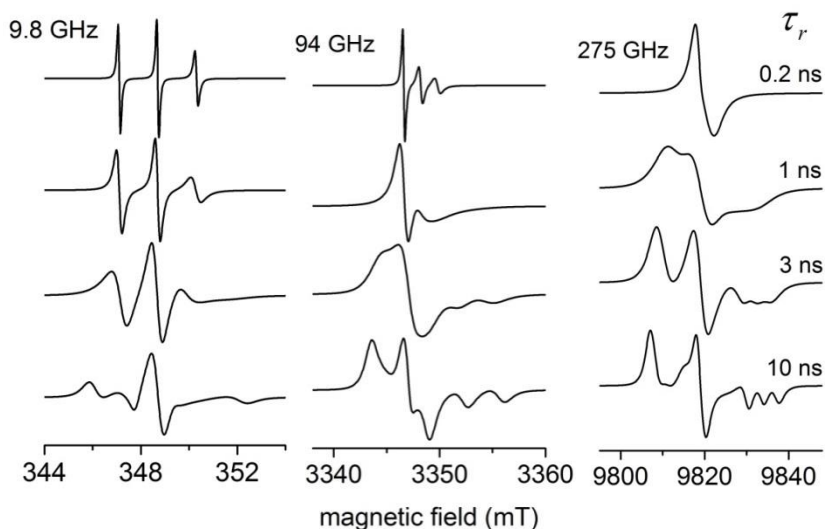


Figure 1.5 Simulations of EPR spectra in the regime of slow molecular tumbling with isotropic values for τ_r . The spectra show the effect of different values for τ_r (0.2, 1, 3, and 10 ns) on the width and position of lines for three microwave frequencies: 9.8, 94.0, and 275.7 GHz. All simulations were done using the EasySpin software package^[19] with the algorithm *Chili*, using a Lorentzian linewidth of 0.1 mT, a hyperfine coupling of $[A_{xx} A_{yy} A_{zz}] = [16.0 \ 15.0 \ 104.1]$ MHz, and a g tensor of $[g_{xx} \ g_{yy} \ g_{zz}] = [2.0088 \ 2.0061 \ 2.0027]$.

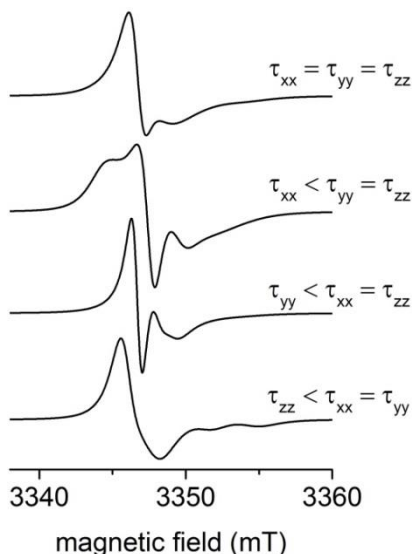


Figure 1.6 Simulations of EPR spectra at 94.0 GHz in the regime of slow molecular tumbling with anisotropic values for τ_r . The bottom three spectra represent results with one fast component (0.7 ns) and two slow components (2.8 ns). For comparison, the top spectrum was simulated with an isotropic τ_r of 1.4 ns. The other simulation parameters used were as mentioned in the caption of Figure 1.5.

1.3 Relaxation of electron spins

The population of the levels $m_s = +\frac{1}{2}$ and $m_s = -\frac{1}{2}$ is governed by the Boltzmann distribution. At room temperature, the difference between the populations is very small, since the magnetic energy is much smaller than the thermal energy. Nevertheless, this difference is responsible for the detection of the EPR signal. The absorption of microwaves can equalize the population of the magnetic levels, causing the EPR signal to disappear. Relaxation, however, brings the system back to the Boltzmann populations and allows for a continuous detection of the EPR signal.

Longitudinal and transverse relaxation, T_1 and T_2

In the presence of an external magnetic field aligned along the z -axis, a collection of spins has at thermal equilibrium a bulk magnetization vector \vec{M} directed along the z -axis. When \vec{M} is perturbed, longitudinal relaxation causes \vec{M} to be restored along the z -axis. This process involves a loss of magnetic energy, which is dissipated as heat to the environment. The time in which 63% ($1 - e^{-1}$) of the z -component of the magnetization is restored is called T_1 and can be measured by pulse EPR using the sequence $\pi - t - (\pi/2) - \tau - \pi - \tau - [\text{echo}]$, where t is the increment time and τ is the delay time.

Transverse relaxation causes the decay of \vec{M} in the transversal (xy) plane. In contrast to longitudinal relaxation, the transversal relaxation does not lead to a loss of magnetic energy of the spins. The time in which the x - (or y -) component of the magnetization decays to 37% is called T_2 and can be measured by the pulse sequence $(\pi/2) - \tau - \pi - \tau - [\text{echo}]$.

Measurement of T_1 and T_2 by microwave saturation

Pulse measurements may not always be feasible to measure the T_1 and T_2 of a sample. An alternative is offered by microwave saturation, which was recognized in early studies by Portis^[20] and Castner^[21]. A saturation curve is obtained in cw mode by measuring the amplitude Y of a first-derivative EPR line (Figure 1.7) as a function of the microwave power P . At low microwave power Y increases linearly with \sqrt{P} , while Y decreases for higher microwave powers. The loss of amplitude at higher microwave power results from saturation. Figure 1.8 shows an example of a saturation curve. The value $P_{1/2}$ is characteristic for a saturation curve and is defined as the microwave power, at which Y is half of the unsaturated value. The shape of the saturation curve is, amongst others, determined by the product $T_1 T_2$ ^[22]:

$$Y \propto \frac{B_1}{(1 + B_1^2 \gamma^2 T_1 T_2)^\varepsilon}, \quad (1.8)$$

where B_1 is the microwave magnetic field, $\gamma = g_e \mu_B / \hbar$, and ε is a measure for the homogeneity of the saturation. For a homogeneously broadened (Lorentzian) line, $\varepsilon = 1.5$. For an inhomogeneously broadened (Gaussian) line, $\varepsilon = 0.5$. Measurement of the amplitude Y as a function of microwave power (B_1^2) allows the determination of the product of T_1 and T_2 .

Figure 1.7 First-derivative EPR line with a peak-to-peak amplitude Y and a peak-to-peak linewidth δ .

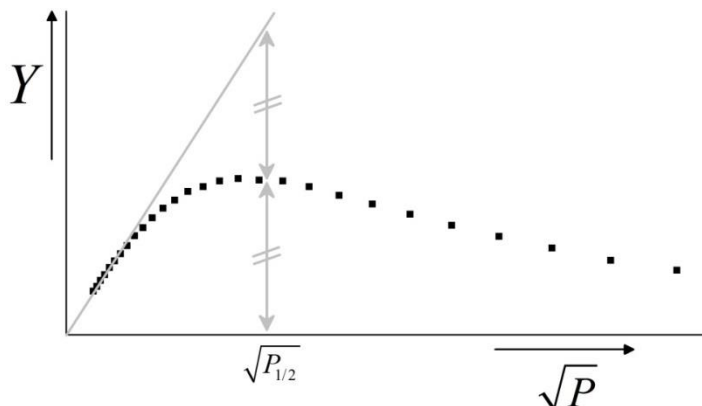
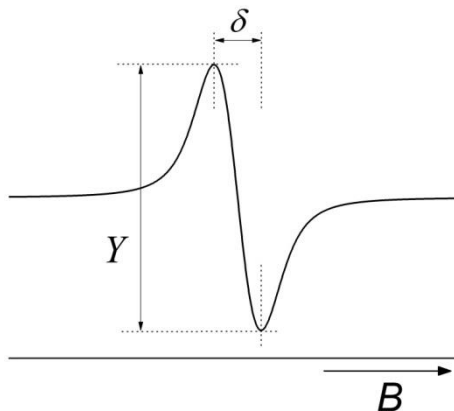


Figure 1.8 An example of a saturation curve. At low microwave power, Y increases linearly with \sqrt{P} . At higher microwave powers, saturation occurs, causing Y to decrease. The value $P_{1/2}$ is defined as the microwave power at which Y is half of the unsaturated value.

1.4 Spin-spin interactions

Spin-spin interactions are detected by EPR, if two unpaired electrons, at sites A and B, are sufficiently close. Hence, spin-spin interactions may serve as indication for the proximity of the electrons. Two terms in spin-spin

interactions are distinguished: exchange interaction and dipole-dipole interaction.

Exchange interaction

Exchange interaction arises from the overlap between electronic wavefunctions. The exchange Hamiltonian is

$$\mathcal{H}_e = -2J\vec{S}_A \cdot \vec{S}_B, \quad (1.9)$$

where J is the exchange energy. The eigenfunctions of \mathcal{H}_e are the $S = 0$ (singlet) and $S = 1$ (triplet) spin functions, where S refers to the total spin of the two electrons.

We shall consider the regime of fast molecular tumbling. Additionally, we take into account the Zeeman interaction and the hyperfine interaction of the electron spins with two ^{14}N nuclear spins ($I = 1$). The eigenvalues of the singlet and the three triplet spin functions are

$$\begin{aligned} (\text{triplet}) \quad & |\beta_A \beta_B\rangle & \frac{1}{4}J + g\mu_B B + \frac{1}{2}aM_I \\ (\text{triplet}) \quad & \frac{1}{\sqrt{2}}|\alpha_A \beta_B + \beta_A \alpha_B\rangle & -\frac{1}{4}J + \frac{1}{2}\sqrt{a^2(\Delta m_i)^2 + J^2} \\ (\text{singlet}) \quad & \frac{1}{\sqrt{2}}|\alpha_A \beta_B - \beta_A \alpha_B\rangle & -\frac{1}{4}J - \frac{1}{2}\sqrt{a^2(\Delta m_i)^2 + J^2} \\ (\text{triplet}) \quad & |\alpha_A \alpha_B\rangle & \frac{1}{4}J - g\mu_B B - \frac{1}{2}aM_I \end{aligned} \quad (1.10)$$

with

$$M_I = m_i^A + m_i^B \quad \text{and} \quad \Delta m_i = m_i^A - m_i^B. \quad (1.11)$$

The total quantum number M_I splits up the state $|\alpha_A\alpha_B\rangle$ and $|\beta_A\beta_B\rangle$ into five levels ($M_I = -2, -1, 0, +1, +2$). The square of the difference in nuclear quantum numbers $(\Delta m_i)^2$ splits up the states $\frac{1}{\sqrt{2}}|\alpha_A\beta_B + \beta_A\alpha_B\rangle$ and $\frac{1}{\sqrt{2}}|\alpha_A\beta_B - \beta_A\alpha_B\rangle$ into three levels ($|\Delta m_i| = 0, 1, 2$). With the selection rule $\Delta m_s = \pm 1$, the allowed transitions are:

$$\begin{aligned}
\frac{1}{\sqrt{2}}|\alpha_A\beta_B + \beta_A\alpha_B\rangle &\leftrightarrow |\beta_A\beta_B\rangle & h\nu &= \frac{1}{2}J + g\mu_B B + \frac{1}{2}aM_I - \frac{1}{2}\sqrt{a^2(\Delta m_i)^2 + J^2} \\
\frac{1}{\sqrt{2}}|\alpha_A\beta_B + \beta_A\alpha_B\rangle &\leftrightarrow |\alpha_A\alpha_B\rangle & h\nu &= -\frac{1}{2}J + g\mu_B B + \frac{1}{2}aM_I + \frac{1}{2}\sqrt{a^2(\Delta m_i)^2 + J^2} \\
\frac{1}{\sqrt{2}}|\alpha_A\beta_B - \beta_A\alpha_B\rangle &\leftrightarrow |\beta_A\beta_B\rangle & h\nu &= \frac{1}{2}J + g\mu_B B + \frac{1}{2}aM_I + \frac{1}{2}\sqrt{a^2(\Delta m_i)^2 + J^2} \\
\frac{1}{\sqrt{2}}|\alpha_A\beta_B - \beta_A\alpha_B\rangle &\leftrightarrow |\alpha_A\alpha_B\rangle & h\nu &= -\frac{1}{2}J + g\mu_B B + \frac{1}{2}aM_I - \frac{1}{2}\sqrt{a^2(\Delta m_i)^2 + J^2}
\end{aligned} \tag{1.12}$$

In the weak exchange regime, i.e., for $|J| \ll a$, the four equations in equation 1.12 reduce to the form of equation 1.6, which is the resonance condition for non-interacting electron spins. A three-line spectrum, such as shown in Figure 1.4, results.

In the strong exchange regime, i.e., for $|J| \gg a$, the term $\frac{1}{2}\sqrt{a^2(\Delta m_i)^2 + J^2}$ in equation 1.12 reduces to $\frac{1}{2}J$. In this regime the singlet-triplet transitions are forbidden and the allowed triplet-triplet transitions occur for

$$h\nu = g\mu_B B + \frac{1}{2}aM_I. \tag{1.13}$$

Figure 1.9 shows the energy levels and the triplet-triplet transitions for two electron spins in the strong exchange regime. Owing to different combinations of m_i^A and m_i^B the energy levels of states $|\alpha_A\alpha_B\rangle$ and $|\beta_A\beta_B\rangle$ are one-, two-,

three-, two-, and one-fold degenerate. Therefore, the spectrum contains five lines, which have 1:2:3:2:1 relative line amplitudes (Figure 1.10). The spectral lines are spaced by $\frac{1}{2}a$.

More complex spectra are expected for systems in the intermediate exchange regime, i.e., for $|J| \sim a$.

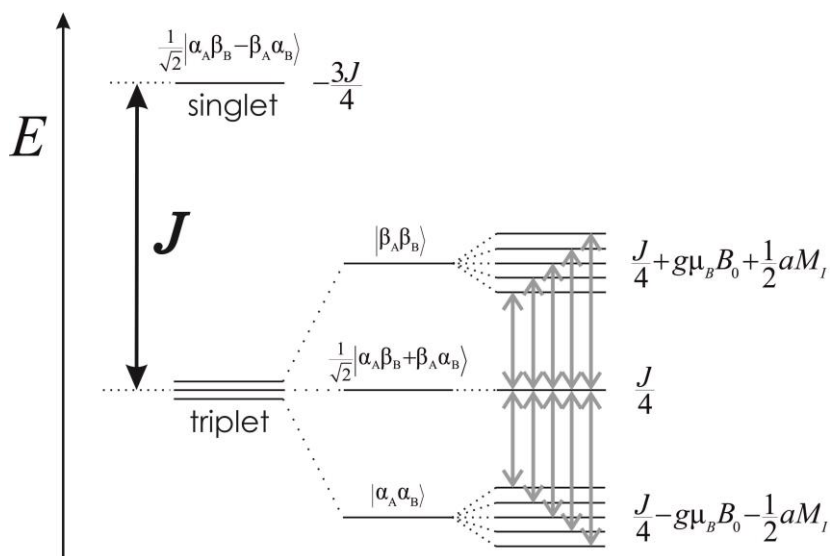


Figure 1.9 Schematic energy diagram of two electron spins (in singlet and triplet state) in the strong exchange regime. The degree of coupling between the electron spins is given by the exchange energy (J). Also, the effect is shown of electron spins interacting with an external magnetic field and with a ^{14}N nuclear spin ($I = 1$). The grey arrows indicate the allowed triplet-triplet transitions.

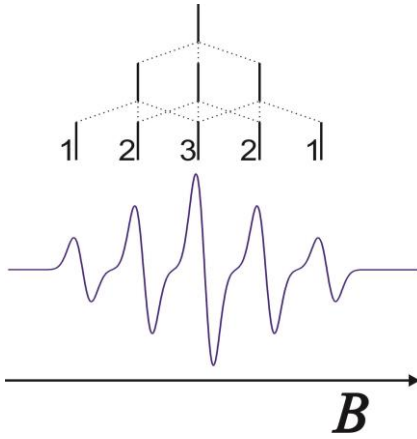


Figure 1.10 An example of a cw-EPR spectrum containing five lines as a result of two interacting electron spins in the strong exchange regime, coupled to two $I = 1$ nuclei. The EPR lines have 1:2:3:2:1 relative amplitudes and correspond to the transitions depicted in the energy diagram of Figure 1.9.

Dipole-dipole interaction

The dipole-dipole coupling ω_{dd} between two spins (g values g_1 and g_2) is proportional to the inverse cube of the distance r and is given by^[13]

$$\omega_{dd}(\theta, r) = \frac{2\pi g_1 g_2}{g_e^2} (3\cos^2\theta - 1) \frac{52.04}{r^3} [\text{MHz nm}^3], \quad (1.14)$$

where g_e is the g value of the free electron. The angle θ is the angle of the spin-spin vector and the magnetic field. For distances up to about 2 nm, dipolar broadening in cw spectra allows for a distance determination by lineshape analysis^[24]. Pulse EPR-techniques^[23] can access distances in the range of 2 – 6 nm or, in favourable cases, even up to 8 nm^[13;25].

To determine distances larger than 2 nm, the most widely used technique is the four-pulse double electron-electron resonance (DEER) experiment^[26]. This experiment consists of the pulse sequence

$$(\pi/2)_{obs} - \tau_1 - (\pi)_{obs} - (\tau_1 + t) - (\pi)_{pump} - (\tau_2 - t) - (\pi)_{obs} - \tau_2 - [\text{echo}],$$

where the subscripts *obs* and *pump* indicate pulses occurring at the observer

and pump frequency. The sequence is illustrated in Figure 1.11a. The measured DEER trace (Figure 1.11b) can be analysed with the proper software^[27] to convert the time-domain signal into a distance distribution (Figure 1.11c).

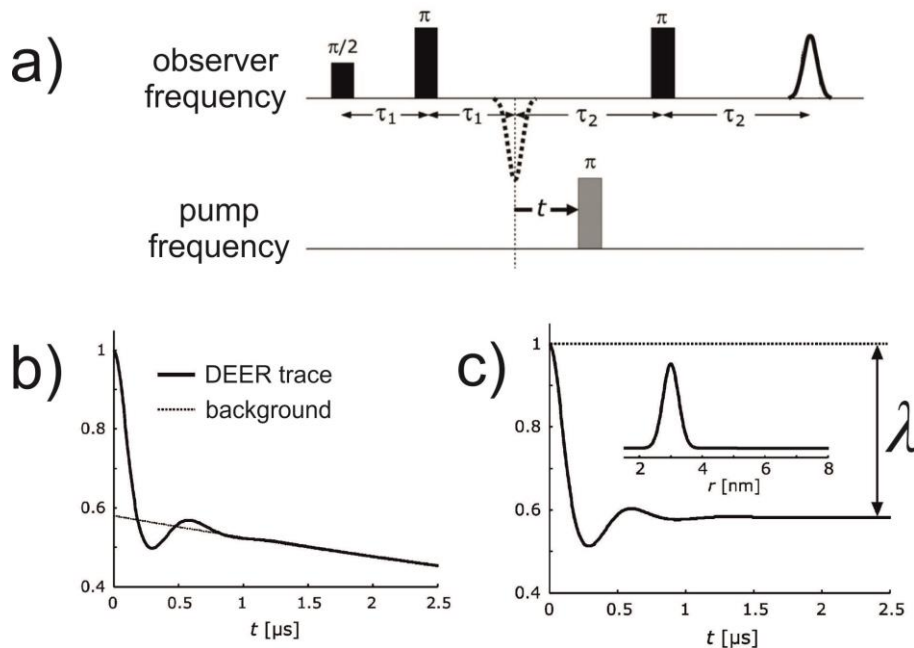


Figure 1.11 The DEER experiment and data analysis. a) The DEER experiment is achieved by a four-pulse sequence at two frequencies that are ~ 65 MHz apart. Delay times τ_1 and τ_2 are kept fixed, while delay time t between the unobserved first echo (dotted line) and the pump pulse is varied. b) The measured DEER trace is the integrated intensity of the observed echo as a function of the dipolar evolution time t . The trace contains a modulation, which is the result of the dipolar coupling between two electron spins. Once the DEER trace is corrected for the background, c) the modulation can be transformed into a distance distribution, which, for this trace, is shown in the inset. The modulation depth (λ) is related to the number of spins that account for the measured DEER trace. The figures concern an edited version of those in reference [25].

1.5 Scope of thesis

This section gives a brief overview of the subjects studied in this work.

In *Chapter 2*, continuous-wave EPR at 9 GHz is used to study the complex formation of E and K peptides, which mimic essential parts of proteins that facilitate membrane fusion. The spectral changes upon mixing of the E and K peptides show that the heterodimer formation can indeed be detected by EPR.

In *Chapter 3*, all three experimental EPR frequencies available at Leiden Institute of Physics (9, 94, and 275 GHz) are used to study the complex of cytochrome *c* peroxidase with spin-labelled cytochrome *c*. The combination of EPR measurements, spectral simulations and principal component analysis allows for a quantitative analysis of the immobilization of the spin label upon complex formation of the proteins.

In *Chapter 4*, microwave-power saturation is used to study the relaxation behaviour of the paramagnetic centre of TOAC in doubly labelled 3_{10} -helical peptides. This work demonstrates that in the doubly labelled peptides the exchange interaction J causes additional relaxation of the paramagnetic centres compared to mono-labelled peptides.

In *Chapter 5*, the unfolding of a doubly labelled protein is studied by the four-pulse DEER experiment. A folding intermediate is revealed by the analysis of the distance distributions.

References

- [1] www.rcsb.org/pdb/statistics/contentGrowthChart.do?content=total&seqid=100
- [2] L. Pauling, R.B. Corey, H.R. Branson, The Structure of Proteins - 2 Hydrogen-Bonded Helical Configurations of the Polypeptide Chain. *Proceedings of the National Academy of Sciences of the United States of America* **37** (1951) 205-211.
- [3] F.H.C. Crick, The Packing of Alpha-Helices - Simple Coiled-Coils. *Acta Crystallographica* **6** (1953) 689-697.
- [4] J.D. Watson, F.H.C. Crick, Molecular Structure of Nucleic Acids - A Structure for Deoxyribose Nucleic Acid. *Nature* **171** (1953) 737-738.
- [5] R.E. Franklin, R.G. Gosling, Molecular Configuration in Sodium Thymonucleate. *Nature* **171** (1953) 740-741.
- [6] N.M. Atherton, Principles of electron spin resonance, Ellis Horwood, Chichester, 1993.
- [7] S.I. Ohnishi, H.M. McConnell, Interaction of Radical Ion of Chlorpromazine with Deoxyribonucleic Acid. *Journal of the American Chemical Society* **87** (1965) 2293.
- [8] T.J. Stone, T. Buckman, P.L. Nordio, H.M. McConnell, Spin-Labeled Biomolecules. *Proceedings of the National Academy of Sciences of the United States of America* **54** (1965) 1010-1017.
- [9] L.J. Berliner, Spin labeling: Theory and Applications, Academic Press, New York, 1976.
- [10] L.J. Berliner, J. Grunwald, H.O. Hankovszky, K. Hideg, A Novel Reversible Thiol-Specific Spin Label - Papain Active-Site Labeling and Inhibition. *Analytical Biochemistry* **119** (1982) 450-455.
- [11] A. Rassat, P. Rey, Nitroxides .23. Preparation of Amino-Acid Free Radicals and Their Complex Salts. *Bulletin de la Societe Chimique de France* (1967) 815-818.
- [12] C.J. Lopez, S. Oga, W.L. Hubbell, Mapping Molecular Flexibility of Proteins with Site-Directed Spin Labeling: A Case Study of Myoglobin. *Biochemistry* **51** (2012) 6568-6583.
- [13] G. Jeschke, Distance measurements in the nanometer range by pulse EPR. *Chemphyschem* **3** (2002) 927-932.
- [14] W.L. Hubbell, C. Altenbach, Investigation of Structure and Dynamics in Membrane-Proteins Using Site-Directed Spin-Labeling. *Current Opinion in Structural Biology* **4** (1994) 566-573.
- [15] C. Altenbach, S.L. Flitsch, H.G. Khorana, W.L. Hubbell, Structural Studies on Transmembrane Proteins .2. Spin Labeling of Bacteriorhodopsin Mutants at Unique Cysteines. *Biochemistry* **28** (1989) 7806-7812.
- [16] P. Zeeman, The Effect of Magnetisation on the Nature of Light Emitted by a Substance. *Nature* **55** (1897) 347.
- [17] sites.google.com/site/altenbach/labview-programs/epr-programs/
- [18] D.E. Budil, S. Lee, S. Saxena, J.H. Freed, Nonlinear-least-squares analysis of slow-motion EPR spectra in one and two dimensions using a modified Levenberg-Marquardt algorithm. *Journal of Magnetic Resonance Series A* **120** (1996) 155-189.
- [19] S. Stoll, A. Schweiger, EasySpin, a comprehensive software package for spectral simulation and analysis in EPR. *Journal of Magnetic Resonance* **178** (2006) 42-55.

- [20] A.M. Portis, Electronic Structure of F-Centers - Saturation of the Electron Spin Resonance. *Physical Review* **91** (1953) 1071-1078.
- [21] T.G. Castner, Saturation of the Paramagnetic Resonance of A V-Center. *Physical Review* **115** (1959) 1506-1515.
- [22] C.P. Poole, *Electron Spin Resonance*, Wiley, New York, 1983.
- [23] G. Jeschke, Determination of the nanostructure of polymer materials by electron paramagnetic resonance spectroscopy. *Macromolecular Rapid Communications* **23** (2002) 227-246.
- [24] A. Schweiger, G. Jeschke *Principles of pulse electron paramagnetic resonance*, Oxford University Press, New York, 2001.
- [25] G. Jeschke, Y. Polyhach, Distance measurements on spin-labelled biomacromolecules by pulsed electron paramagnetic resonance. *Physical Chemistry Chemical Physics* **9** (2007) 1895-1910.
- [26] M. Pannier, S. Veit, A. Godt, G. Jeschke, H.W. Spiess, Dead-time free measurement of dipole-dipole interactions between electron spins. *Journal of Magnetic Resonance* **142** (2000) 331-340.
- [27] G. Jeschke, V. Chechik, P. Ionita, A. Godt, H. Zimmermann, J. Banham, C.R. Timmel, D. Hilger, H. Jung, DeerAnalysis2006 - a comprehensive software package for analyzing pulsed ELDOR data. *Applied Magnetic Resonance* **30** (2006) 473-498.

2

HETERODIMER FORMATION OF MEMBRANE-FUSION E/K PEPTIDES STUDIED BY CONTINUOUS-WAVE EPR

2.1 Introduction

Membrane fusion is an essential process in living organisms. In eukaryotic cells, the early stage of fusion involves two membranes, each with a membrane-anchored SNARE protein^[1] (SNARE, soluble NSF attachment protein receptor; NSF = N-ethylmaleimide-sensitive factor). The mechanism of membrane fusion is still unknown^[2]. To investigate membrane fusion involving SNARE proteins, model systems are synthetically designed, which mimic the biological system. The building blocks are biologically inspired modules and consist of a membrane anchoring segment, a zipper segment, and a linker that connects the two segments (Figure 2.1a). To understand whether the final construct will be functional in membrane fusion, it is important to know how the components operate by themselves. In this study, we concentrate on the zipper segment, i.e., peptides that self-assemble into a coiled-coil^[3] complex, similarly to the zipper segment of SNARE proteins.

Inspired by the work of Litowski and Hodges^[4:5], we synthesized variants of the oligopeptides E and K, listed in Table 2.1. The E and K peptides are oppositely charged, due to the abundant glutamic acid (E) and lysine (K) residues, respectively. Figure 2.1b shows the ionic and hydrophobic

interactions, which are expected to stabilize the heterodimer. A tryptophan (W) and a tyrosine (Y) residue were incorporated to facilitate the use of UV-Vis spectroscopy to determine the concentration of the peptide. Under physiological conditions, peptide E adopts a predominantly random-coil conformation, while peptide K is predominantly α -helical^[6]. When mixed, peptides E and K are designed to twist around one another to form a coiled-coil^[4]. With only three heptad repeats, they are the shortest known coiled-coil pair, which assembles specifically into a stable heterodimer ($K_D \sim 10^{-7}$ M at 25 °C)^[4-6]. For our variants specifically, the E and K peptides form heterodimers in parallel fashion, with all of the residues participating in the coiled-coil^[7].

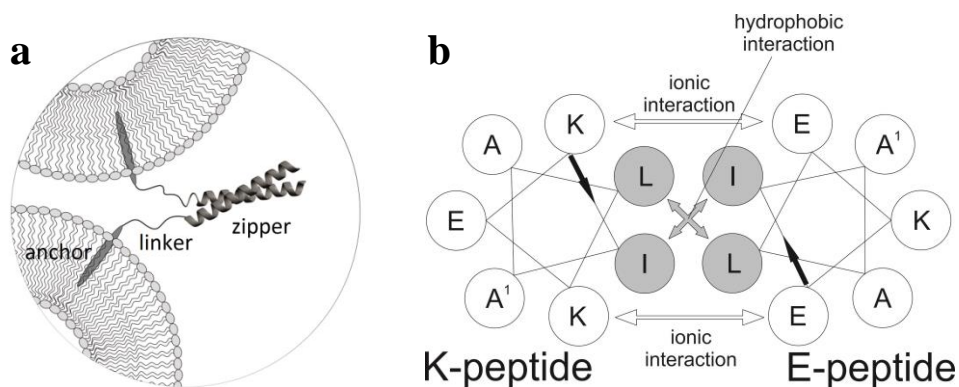


Figure 2.1: Schematic representations of: **a)** a membrane-fusion construct consisting of a zipper segment, a linker, and a membrane anchor; **b)** the K- and E-peptides in a helical wheel projection. The peptides propagate into the page from the N-terminus to the C-terminus. The repeating leucine (L) and isoleucine (I) residues form a hydrophobic face along both peptides^[8]. Their side chains interact with each other (grey arrows) in a “knobs-into-hole”^[5;9] manner, forming a continuous hydrophobic core. Ionic attractions between glutamic acid (E) and lysine (K) make the interaction selective.

In the present work we assess to what extent mobility information from room-temperature spin-label EPR^[10;11] can be used to study dimer formation of the E/K peptides. To do so, a cysteine residue was introduced and the peptide was coupled to an MTSL label^[12] (Figure 2.2). All investigated peptides are listed in Table 2.1. We use the abbreviations SL-K for the K peptide with the spin label (SL) attached at the N-terminus, and E-SL and K-SL for the E and K peptides, respectively, when the spin label is attached at the C-terminus. An accompanying study shows that the spin label does not change the secondary structure of the peptides, nor that it disturbs the self-assembly of the E/K peptide pair^[7]. Advantages of spin-label EPR are that heterodimer formation can be detected *in situ* and in the presence of membranes.

Table 2.1 Peptide sequences

peptide	sequence
E-SL	Ac-(EIAALEK) ₃ -GYC(SL)-NH ₂
K-SL	Ac-(KIAALKE) ₃ -GWC(SL)-NH ₂
SL-K	Ac-C(SL)-(KIAALKE) ₃ -GW-NH ₂
E	Ac-(EIAALEK) ₃ -GY-NH ₂
K	Ac-(KIAALKE) ₃ -GW-NH ₂

C(SL) = cysteine with MTSL attached, Ac = acetyl

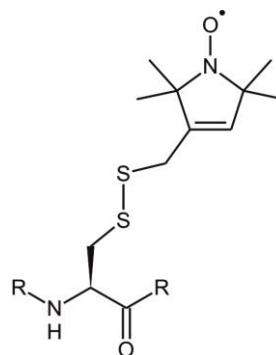


Figure 2.2 Chemical structure of the spin-label MTSL attached to a cysteine residue in a peptide.

In this study we use two approaches. We mix the spin-labeled peptide with its unlabeled partner peptide (e.g. E-SL with K), expecting a mobility decrease upon heterodimer formation. As a control, we mix the spin-labeled peptide with its unlabeled twin peptide (e.g. E-SL with E). Any mobility change due to unspecific interaction or viscosity changes should be revealed by the latter

experiment. In the second approach, we investigate samples in which both partners are labeled, to detect potential spin-spin interaction owing to the close approach of the spin labels.

We show that heterodimer formation can be detected by the mobility change in EPR. The absence of spin-spin interaction in the SL-K:E-SL pair and E-SL:K-SL pair puts a structural constraint on the heterodimer: a minimal distance of 0.8 nm between the two electron spins. The present work paves the road for future EPR studies on the peptides E and K integrated into more complex systems.

2.2 Material and methods

The synthesis of the peptides listed in Table 2.1 was done by Tingting Zheng (Supramolecular & Biomaterials Chemistry group at Leiden Institute of Chemistry) and has been described elsewhere^[7].

EPR measurements

The cw-EPR measurements were performed at 9.8 GHz using an ELEXSYS E 680 spectrometer (Bruker BioSpin GmbH, Rheinstetten, Germany) equipped with a rectangular cavity. All spectra were recorded at a microwave power of 0.63 mW with a field sweep of 15 mT and 2048 field points. Field modulation at a frequency of 100 kHz was employed with an amplitude of 0.04 mT. The measurement time was 20 minutes per sample. The time constant was 2.56 ms with a conversion time of 5.12 ms. The temperature was 293 ± 1 K.

Solutions were contained in 50 μ L micropipettes (BLAUBRAND[®] intraMARK) with an inner/outer diameter of 0.80/1.50 mm. Samples were prepared in phosphate buffered saline (PBS), pH 7.4. The measurements done are summarized in three categories: a sample of (i) labeled peptide, 150 μ M, and mixtures of (ii) labeled peptide with non-labeled peptide, both 100 μ M, and (iii) labeled peptide with labeled peptide, both 100 μ M. Peptide concentrations for category (i) and (ii) were based on UV-Vis absorption. For category (iii) spin concentrations were used (see below). A quantitative analysis of the spin-label concentration was made by double integration of the EPR spectrum and comparison to the spectrum of a reference sample with known spin concentration. Based on this analysis, we found that more than 80% of the peptides E-SL, K-SL, and SL-K gave an EPR signal, i.e., were effectively spin labeled.

To check whether the peptide influences the solution viscosity, we also measured a sample of the spin label (MTSL) alone and in the presence of 200

μM of peptide E. Similarly, peptide E-SL was measured at concentrations between 100 μM and 200 μM in increments of 25 μM .

Simulation of EPR spectra

Simulations of cw-EPR spectra were done with EasySpin^[13], a software package for MATLAB (The Mathworks, Natick, MA, USA). The function *Garlic* was combined with the isotropic rotation model. The spin system was defined by tensors $\bar{\bar{g}} = [g_{xx} \ g_{yy} \ g_{zz}] = [2.0078 \ 2.0058 \ 2.0023]$ and $\bar{\bar{A}}_N = [A_{xx} \ A_{yy} \ A_{zz}] = [5.99 \ 5.99 \ 36.38]$ MHz. The hyperfine tensor $\bar{\bar{A}}_N$ derives from the interaction of the electron spin with the ^{14}N ($I = 1$) nucleus. A second component was added (5%) to account for the satellite lines due to coupling of the electron spin with ^{13}C ($I = 1/2$) nuclei in natural abundance. For this fraction $\bar{\bar{A}}_C = [A_{xx} \ A_{yy} \ A_{zz}] = [6.63 \ 6.63 \ 6.63]$ MHz was used. Within a series of simulations concerning one particular labeled peptide (e.g. E-SL, E-SL:E, or E-SL:K), the lineshape parameters were kept constant. The simulated spectrum was adjusted to the experimental one varying the rotation-correlation time. We used visual inspection to make the simulated spectrum resemble the experimental spectrum.

Rotation-correlation time

We assume that the line shape of the EPR spectrum, described by the rotation-correlation time τ_r , derives from a combination of the local mobility of the spin label ($\tau_{r,\text{local}}$) and overall peptide motion $\tau_{r,\text{peptide}}$

$$\frac{1}{\tau_r} = \frac{1}{\tau_{r,\text{peptide}}} + \frac{1}{\tau_{r,\text{local}}} \quad (2.1)$$

To calculate the rotation-correlation time of the peptide $\tau_{r,\text{peptide}}$, the Stokes-Einstein equation

$$\tau_{r,\text{peptide}} = \frac{\eta V}{k_B T} \quad (2.2)$$

is used, where η is the solution viscosity, for water 1.00 mP·s, k_B is the Boltzmann constant, and T is the temperature, in this work: 293 ± 1 K. The volume V of the E and K peptides is described by cylinders with a length of 3.9 nm and a diameter of 1.1 nm. The volumes are 3.7 nm^3 for the monomeric peptide and 7.4 nm^3 for the heterodimer. From equation 2.2, $\tau_{r,\text{peptide}} = 0.92$ ns for a monomeric peptide and $\tau_{r,\text{peptide}} = 1.83$ ns for a heterodimer are obtained.

Averaging of dipole-dipole interaction

For a system containing two unpaired electron spins, the dipole-dipole interaction is averaged by molecular tumbling if

$$\omega_{dd} < \frac{2\pi}{\tau_r}. \quad (2.3)$$

The dipole-dipole coupling between two spins is proportional to the inverse cube of the distance^[14]

$$\omega_{dd}(\theta, r) = \frac{2\pi g_1 g_2}{g_e^2} (3 \cos^2 \theta - 1) \frac{52.04}{r^3} [\text{MHz nm}^3]. \quad (2.4)$$

See Section 1.4 for the clarification of the symbols used in equation 2.4.

For $\tau_r = 1.83$ ns an upper limit of $\omega_{dd} = 546 \cdot 10^6$ rad/s results, which corresponds to a distance of 0.8 nm.

2.3 Results

Figure 2.3 shows the EPR spectrum of E-SL:E superimposed on the spectrum of E-SL:K. The spectra are superimposed such that the middle one of the three EPR lines overlaps optimally. The high-field line in the spectrum of E-SL:K is broadened compared to E-SL:E. A similar feature is observed in the spectra of the samples in which K-SL or SL-K are mixed with their partner peptides (data not shown).

Control experiments show that the spectrum of the free spin label is not influenced by the presence of different concentrations of peptide (see Material and methods). Also, the spectral lineshape of peptide E-SL does not change within the signal-to-noise ratio for samples where the concentration of E or E-SL is varied.

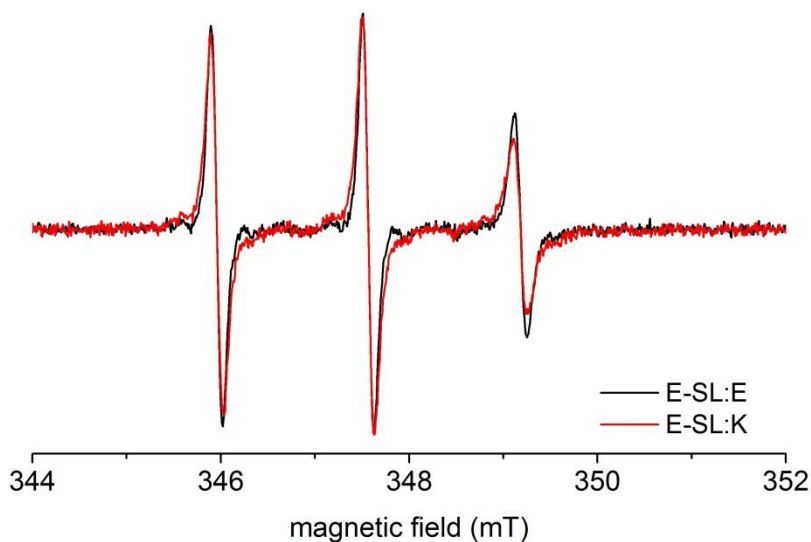


Figure 2.3: The room temperature cw-EPR spectrum of E-SL:E (in black) superimposed on E-SL:K (in red).

In total nine combinations of peptides were measured (see Table 2.2). Simulations were performed with a model of isotropic rotation. The simulated spectra agree well with the experimental spectra, i.e., within the noise amplitude. The exception is the simulated spectrum of SL-K:E. Here the amplitude of the low-field line even in the best-matched simulation was 7% larger and the high-field line was 28% broader than the experimental spectrum. The parameters obtained by the simulations are the rotation-correlation times (τ_r) and linewidths given in Table 2.2.

Table 2.2 Parameters used for the simulation of EPR spectra.

simulation	linewidth ^a (mT)	τ_r ^b (ps)
E-SL	0.11 – 0.02	158
E-SL:E	0.11 – 0.02	186
E-SL:K	0.11 – 0.02	307
K-SL	0.10 – 0.04	169
K-SL:K	0.10 – 0.04	181
K-SL:E	0.10 – 0.04	236
SL-K	0.09 – 0.07	197
SL-K:K	0.09 – 0.07	200
SL-K:E	0.09 – 0.07	269

^a The spectral lines were best described using a mixture of Gaussian and Lorentzian lineshapes. The first and second value correspond to the width of the Gaussian and Lorentzian line, respectively.

^b The rotation-correlation time was determined with an error of ± 15 ps.

Considering the three samples with E-SL, the τ_r values of E-SL and E-SL:E agree within the experimental error, whereas the τ_r of E-SL:K is significantly larger. The same is true for samples containing K-SL and SL-K. The increase in τ_r is largest for E-SL, i.e., from 158 (E-SL) to 307 ps (E-SL:K), and

smallest for K-SL. Amongst the heterodimers, τ_r is largest for E-SL:K (307 ps) and smallest for K-SL:E (236 ps).

Figure 2.4 shows the overlay of the spectrum of E-SL:K-SL and the suitable reference spectrum. Similarly for E-SL:SL-K (Figure 2.5). The spectra of samples in which both partners are labeled are identical within the noise to their respective reference spectra.

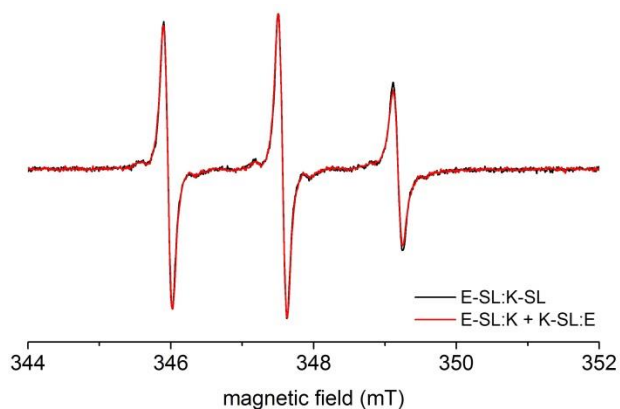


Figure 2.4: The spectrum of E-SL:K-SL (in black) superimposed on the sum of the spectra of E-SL:K and SL-K:E (in red).

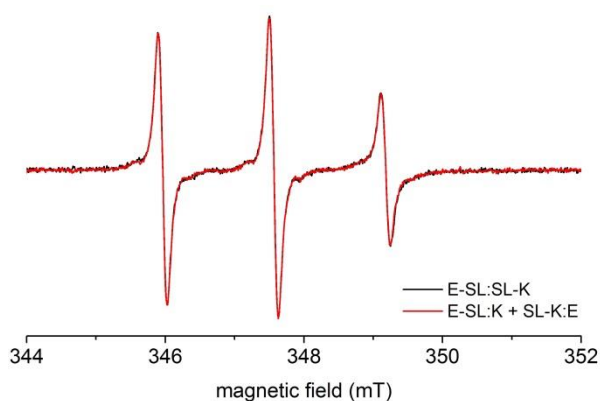


Figure 2.5: The spectrum of E-SL:SL-K (in black) superimposed on the sum of the spectra of E-SL:K and SL-K:E (in red).

2.4 Discussion

To investigate heterodimer formation in the E/K peptides we determined the mobility of the spin label in a set of combinations of these peptides (Table 2.2). In almost all cases, an isotropic rotational model was sufficient to simulate the mobility of the spin label showing that neither monomers nor dimers have preferential axes of rotation. A significant increase of τ_r is found in all cases where the heterodimers are formed, irrespective of the position of spin-label attachment (N- or C-terminus, E or K peptide), showing that mobility measurements by cw-EPR provides a valid method to detect dimer formation in the E/K peptides. A set of control experiments shows that the peptides do not significantly influence the τ_r via viscosity changes of the solution. Significant changes in τ_r between a spin labeled peptide in the absence and presence of a non-labeled peptide are therefore considered to be caused by peptide-peptide interaction.

How do the observed τ_r values relate to the rotation of the peptide? The measured τ_r values are significantly smaller than those expected for the rotation of the peptide itself, i.e., 0.92 ns for peptide K and 1.83 ns for the heterodimer (see Material and methods). Using equation 2.1, the contribution of peptide rotation ($\tau_{r,\text{peptide}}$) to τ_r is in the order of 20%, revealing that τ_r is largely determined by local mobility, i.e., rotation of the nitroxide about the single bonds joining it to the peptide and/or the mobility in the peptide backbone (Figure 2.2).

Consequently, the τ_r changes reveal that the local mobility decreases when heterodimers are formed. The local-mobility change is largest for the C-terminus of the E peptide, and also somewhat larger for the N-terminus of the K peptide than for the C-terminus of K. A possible explanation for the larger τ_r

change in the E peptide compared to the K peptide is that the E peptide, which is partially random coil in solution, has to convert to an α -helix conformation when the heterodimer is formed. The partial random-coil conformation of the E peptide could offer more flexibility to the nitroxide before heterodimer formation, making the total change in τ_r larger than for the K-peptide.

For none of the combinations of spin-labeled peptides (Figures 2.4 and 2.5) spin-spin interactions were observed, showing that spin labels are too far apart to have either exchange or dipolar interaction. Exchange interaction (J) manifests itself as line broadening or in the occurrence of extra lines in the EPR spectrum if $J \geq A_N/2$, in our case at distances < 0.5 nm. Dipolar interaction could be observed if the dipolar interaction ω_{dd} is sufficiently large not to be averaged by molecular tumbling, which for our labels is at distances < 0.8 nm. The absence of any such effect on the spectra of the peptide partners, where both C-termini are labeled (E-SL:K-SL) or where the E-C-terminus and K-N-terminus (E-SL:SL-K) are labeled, shows that the spin labels are separated by more 0.8 nm.

In a parallel dimer, the shortest distance is expected for the E-SL:K-SL pair, in which both spin labels are at the C-terminus. However, even in this situation the distance could be substantial. The helical-wheel projection shows that if the C-terminal residues that follow the third heptad repeat (K-SL: -GWC-SL) complete a full turn, the cysteine residue would position at the site of the first alanine residue (A^1) of the K peptide (Figure 2.1b), respectively the E peptide, i.e., at opposite faces of the helix. Assuming a helix diameter of 1.1 nm and a linker length of 0.5 nm, a distance of ~ 3.2 nm results, which is significantly larger than the distance to which the liquid-solution measurements we performed are sensitive. Therefore, the absence of spin-spin interaction is consistent with the model shown in Figure 2.1b. The present results do not enable us to exclude an anti-parallel arrangement of the heterodimer.

Paramagnetic NMR and Förster resonance energy transfer experiments do provide such evidence^[7].

We can exclude that oligomers are formed in which peptides cover the termini of their partners. Such an arrangement would block spin label motion and lead to correlation times in the order of oligomer rotation.

In conclusion, we find small but significant changes in the mobility of the spin label under conditions where heterodimers are formed. These *in situ* measurements confirm heterodimer formation in solution, showing that the E/K peptides form a complex. The same approach can be applied to the full construct in a vesicle environment enabling the detection of complex formation in the fully assembled fusion construct.

References

- [1] T. Weber, B.V. Zemelman, J.A. Mcnew, B. Westermann, M. Gmachl, F. Parlati, T.H. Sollner, J.E. Rothman, SNAREpins: Minimal machinery for membrane fusion. *Cell* **92** (1998) 759-772.
- [2] R. Jahn, Some classic papers in the field of membrane fusion - a personal view. *Nature Structural & Molecular Biology* **15** (2008) 655-657.
- [3] P. Burkhard, J. Stetefeld, S.V. Strelkov, Coiled coils: a highly versatile protein folding motif. *Trends in Cell Biology* **11** (2001) 82-88.
- [4] J.R. Litowski, R.S. Hodges, Designing heterodimeric two-stranded alpha-helical coiled-coils - Effects of hydrophobicity and alpha-helical propensity on protein folding, stability, and specificity. *Journal of Biological Chemistry* **277** (2002) 37272-37279.
- [5] D.A. Lindhout, J.R. Litowski, P. Mercier, R.S. Hodges, B.D. Sykes, NMR solution structure of a highly stable de novo heterodimeric coiled-coil. *Biopolymers* **75** (2004) 367-375.
- [6] H.R. Marsden, A.V. Korobko, E.N.M. van Leeuwen, E.M. Pouget, S.J. Veen, N.A.J.M. Sommerdijk, A. Kros, Noncovalent triblock copolymers based on a coiled-coil peptide motif. *Journal of the American Chemical Society* **130** (2008) 9386-9393.
- [7] T. Zheng. Dissertation, Leiden University, *to be published*.
- [8] J.M. Mason, K.M. Arndt, Coiled coil domains: Stability, specificity, and biological implications. *Chembiochem* **5** (2004) 170-176.
- [9] F.H.C. Crick, The Packing of Alpha-Helices - Simple Coiled-Coils. *Acta Crystallographica* **6** (1953) 689-697.
- [10] L.J. Berliner, *Spin labeling: Theory and Applications*, Academic Press, New York, 1976.
- [11] N.M. Atherton, *Principles of electron spin resonance*, Ellis Horwood, Chichester, 1993.
- [12] L.J. Berliner, J. Grunwald, H.O. Hankovszky, K. Hideg, A Novel Reversible Thiol-Specific Spin Label - Papain Active-Site Labeling and Inhibition. *Analytical Biochemistry* **119** (1982) 450-455.
- [13] S. Stoll, A. Schweiger, EasySpin, a comprehensive software package for spectral simulation and analysis in EPR. *Journal of Magnetic Resonance* **178** (2006) 42-55.
- [14] G. Jeschke, Distance measurements in the nanometer range by pulse EPR. *Chemphyschem* **3** (2002) 927-932.

3

THE COMPLEX OF CYTOCHROME *C* WITH CYTOCHROME *C* PEROXIDASE STUDIED BY SPIN-LABEL, MULTI-FREQUENCY ELECTRON PARAMAGNETIC RESONANCE

3.1 Introduction

Transient protein-protein complexes are important in biochemical processes, where they often participate in electron transfer. They are designed to provide fast turnover in the crowded cellular environment^[1]. The formation of transient complexes has been demonstrated to involve an encounter complex, in which the proteins are loosely bound such that they are free to sample their respective surfaces^[2], as well as the more tightly bound, stereo-specific complex, which is capable of electron transfer^[3;4]. The process of complex formation is schematically shown in Figure 3.1. Methods are sought to investigate the encounter complex, which is dynamic^[5] and could be decisive in making protein encounters specific. The formation of the encounter complex seems to be governed by long-range electrostatic interactions^[6;7] and in some cases by hydrophobic interactions^[8].

Here we investigate the complex of yeast mitochondrial iso-1-cytochrome *c* (*Cc*) with cytochrome *c* peroxidase (*CcP*), which in yeast is relevant for the removal of hydrogen peroxide. Previously, the interaction of *Cc* with *CcP* has been studied by paramagnetic NMR, revealing that the interaction

of both proteins is best described by an encounter complex that is populated 30% of the time and a stereo-specific complex that is competent for electron transfer and has a 70% occupancy^[3-5;8;10;11].

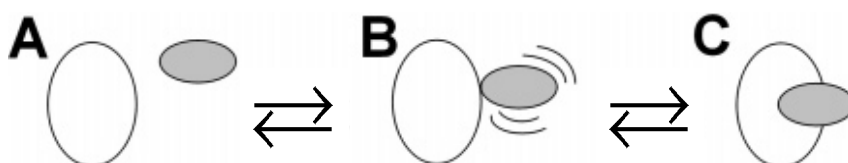


Figure 3.1 A schematic model for the formation of a protein complex. Free partner proteins (A) associate to form an encounter complex (B), in which the proteins are loosely bound such that they are free to sample their respective surfaces. The encounter complex is in equilibrium with a tightly bound stereo-specific complex (C). The figure concerns an edited version of that in reference [9].

We use multi-frequency electron paramagnetic resonance (EPR) at room temperature, where the proteins are in their physiological state, to probe complex formation. The sensitivity of continuous-wave (cw) EPR to the nanosecond motion of a nitroxide spin label covalently attached to the unique cysteine in the A81C mutant of *Cc* (*Cc*-SL) enables us to probe the local environment of this residue.

Previously, cw-EPR has been used to study the high-affinity protein-protein complex of barnase with barstar^[12]. The cw-EPR spectrum of the spin-labelled barnase-barstar complex depends on viscosity, i.e., broad outer peaks of the spin-label signal become more dominant as the viscosity increases^[12]. The combination of cw-EPR^[13;14] and saturation recovery EPR^[13] was applied to the complex of cytochrome *bc*₁ and spin-labelled cytochrome *c*. For this complex formation, it is shown that altering the NaCl concentration in the

buffer affects the cw-EPR spectra, i.e., the width of the outer peaks of the spin-label signal depends on the ionic strength^[13].

We present a systematic approach to analyse a series of EPR spectra obtained at different ratios of the complex partners to determine the dissociation constant. We show how to obtain the spectra of the spin label in the fully-bound state. This is not trivial because the EPR spectra of samples in which both partners are present always contain a fraction in which the spin-labelled partner is not in the complex (free *Cc*-SL), even at a large excess of the complex partner (*CcP*). Since the EPR spectra of free *Cc*-SL and bound *Cc*-SL have significant overlap and cannot be described by a simple lineshape function (Gaussian or Lorentzian), deconvolution is needed.

By monitoring the complex with a spin label attached to the smaller protein of the complex, the changes in rotation-correlation time upon complex formation are maximized. We show that spectra obtained by conventional X-band (9 GHz) EPR are analysed preferably using principal component analysis (PCA)^[15], an approach that is not suited for the high-field, W-band (94 GHz) EPR spectra. To increase spectral resolution even further, EPR at 275 GHz is employed.

We find that the spin label in the A81C-variant of *Cc* becomes immobilized upon complex formation. Two fractions with different mobility of the spin label are observed, which could correspond to the encounter and specific complex, respectively. High-field EPR reveals differences between the free and the fully bound state in the anisotropy of the rotation-correlation time of the spin-label motion. Furthermore, the potential of 275 GHz EPR to increase sensitivity to anisotropic motion is addressed.

3.2 Material and methods

Expression and purification of CcP C128A

The expression and purification of CcP C128A was done by Jesika Schilder (Protein Chemistry group at Leiden Institute of Chemistry), who used a procedure previously described^[16]. The concentration of CcP was determined with UV-Vis spectroscopy: $\epsilon_{408\text{nm}} = 98 \text{ mM}^{-1} \text{ cm}^{-1}$ [17].

Expression and purification of Cc A81C

Chemically competent *E. coli* JM109 cells were freshly transformed with pUC cc A81C plasmid, a pUC18 based plasmid coding for *saccharomyces cerevisiae* Cc A81C. A single colony was used to inoculate 3 ml of 2×YT medium containing 50 µg/ml ampicillin and 1 mM KNO₃, and incubated at 37 °C, 250 rpm until turbidity was evident (3 – 4 hours). One mL of the pre-culture was used to inoculate 1.7 L of 2×YT medium containing 50 µg/mL ampicillin and 1 mM KNO₃ in a 2 L Erlenmeyer flask and incubated at 37°C, 160 rpm for 24 hours. The cells were harvested by centrifugation at 4 °C, 6400 × g for 15 minutes. The pink pellet was re-suspended in a minimum volume of lysis buffer (50 mM Tris-HCl, 1 mM EDTA), flash-frozen in liquid N₂ and stored at –80 °C. After thawing the cells, 3.8 mg DNase and a few milligrams of lysozyme and PMSF were added. The suspension was stirred for 30 minutes at 4°C and twice lysed by a pressure cell homogenizer (FPG12800, Stansted Fluid Power Ltd., Harlow, U.K.). Per mL of solution, 326 mg of (NH₄)₂SO₄ was added. The solution was stirred at 4°C for 30 minutes. Precipitate was removed by centrifugation at 4°C, 9600 × g for 30 min. The supernatant was dialyzed overnight against 5 L of 46 mM NaP_i, pH 6.8. The dialyzed solution was centrifuged at 4°C, 6200 × g for 15 minutes and loaded on a CM column (80 mL) equilibrated with 46 mM NaP_i, pH 6.8 at 2 mL/min. The column was

washed with 46 mM NaP_i, pH 6.8, and with 46 mM NaP_i pH 6.8, 70 mM NaCl for two column volumes. Cc A81C was eluted from the column with 46 mM NaP_i, pH 6.8, 400 mM NaCl, fractions of 2 mL were collected. The fractions showing an absorbance at 550 nm were combined and concentrated to a volume of 2 mL. Dithiothreitol (DTT) was added to the solution to a final concentration of 5 mM. The solution was incubated on ice for 1 hour and run over a Superdex 75 (~ 120 mL) column, pre-equilibrated in 20 mM NaP_i, pH 6.0, 100 mM NaCl, 1 mM DTT, with a flow rate of 1 mL/min, collecting fractions of 1 mL while monitoring the absorption at 280 nm and 550 nm. Fractions with a significant 550 nm signal were combined and concentrated.

This procedure was largely inspired on the procedures described in references [18;19].

Cc A81C spin labelling

Cc A81C (1 mL of 822 µM) was reduced with 5 mM DTT at 4 °C for 60 minutes. DTT was removed with a 5 mL desalting column (GE Healthcare) equilibrated in 100 mM NaP_i, pH 7.2, 100 mM NaCl (argon bubbled to remove oxygen). Immediately after elution, Cc A81C was added to a solution of 20 mL 100 mM NaP_i pH 7.2, 100 mM NaCl, 2.2 mM MTSL. This solution was kept at 4 °C for 1 hour while bubbling with argon. The total volume of 23 mL was concentrated to 0.85 mL and kept overnight at 4 °C. Free MTSL was removed by a Superdex 75 gel filtration column (GE Healthcare) equilibrated in 100 mM NaP_i pH 7.2, 100 mM NaCl, The absorption was monitored at 280, 410, and 550 nm and fractions of 1 mL were collected. Fractions with an A₅₅₀/A₂₈₀ ratio larger than 0.80 were combined and concentrated to 0.7 mL. EPR experiments showed that the spin-labelling efficiency was approximately 93 %. To the protein solution 5 mM K₃[Fe₃(CN)₆] was added. After incubation of 60 minutes, the oxidizing agent was removed by a PD10 column. The protein

solution was concentrated to 0.6 mL. UV-Vis spectroscopy was used to determine the protein concentration of 562 μM ($\epsilon_{410\text{nm}} = 106.1 \text{ mM}^{-1} \text{ cm}^{-1}$ [19]) and to verify that the protein was oxidized. The protein solution was flash frozen in liquid N_2 and stored at -80°C .

Important contributions to this procedure were made by Anneloes Blok (Protein Chemistry group at Leiden Institute of Chemistry).

EPR-sample preparation

All EPR samples were prepared in 20 mM NaP_i , 100 mM NaCl , pH 6.0, with protein concentrations based on UV-Vis absorption. For X-band measurements the samples with 100 μM C_c and varying concentrations of $C_c\text{P}$ were transferred into 50 μL micropipettes (BLAUBRAND[®] intraMARK) with an inner/outer diameter (id/od) of 0.80/1.50 mm. For W-band measurements at room temperature the concentration of spin-labelled C_c was 0.4 mM and samples were placed in suprasil quartz capillaries (Wilmad-Labglass, Buena, NJ, USA) with an id/od of 0.1 mm/0.5 mm. This capillary was put into a suprasil quartz capillary (VitroCom, Mountain Lakes, NJ, USA) with an id/od of 0.60 mm/0.84 mm. At both ends the capillaries were sealed with X-Sealant[®]. For W-band measurements at 80 K the concentration of spin-labelled C_c ($C_c\text{-SL}$) was 0.4 mM and samples were placed in suprasil quartz capillaries (VitroCom, Mountain Lakes, NJ, USA) with an id/od of 0.60 mm/0.84 mm. Both ends were sealed with an epoxy polymer. For the room-temperature measurement at 275 GHz the concentration of $C_c\text{-SL}$ was 3 mM and the sample was measured in a locally made quartz capillary with an id/od of 50 μm /250 μm .

X-band EPR measurements

Measurements at X-band were performed using an ELEXSYS E 680 spectrometer (Bruker BioSpin GmbH, Rheinstetten, Germany) equipped with a rectangular cavity. Spectra were recorded at 0.63 mW microwave power with a modulation amplitude/frequency of 0.2 mT/100 kHz. A 15 mT field sweep of 2048 points was used with a time constant of 10 ms. The total measurement time for a spectrum varied between 35 and 80 minutes. A gentle stream of N₂ was blown through the cavity. A chrome/alumel thermocouple was installed close to the sample to monitor the temperature with a readability of 0.1 K. The temperature during the X-band measurements was 292.6 ± 0.1 K. The buffer in all measurements was 20 mM NaPi, pH 6.0. This buffer had 100 mM NaCl, unless stated otherwise.

EPR measurements at 94 and 275 GHz

For W-band measurements at room temperature and 80 K a locally developed probe head was used combined with a Bruker Elexsys 680 (Bruker BioSpin GmbH, Rheinstetten, Germany) spectrometer. The room-temperature measurement at 275 GHz was done on a locally developed spectrometer [20;21]. Measurements were performed with a modulation amplitude of 0.3 mT (94 GHz, RT), 0.2 mT (94 GHz, 80 K) and 0.6 mT (275 GHz, RT) and a modulation frequency of 10 kHz (94 GHz, RT and 80 K) and 1.7 kHz (275 GHz, RT). The time constant was 82 ms (94 GHz, RT), 41 ms (94 GHz, 80 K) and 1 s (275 GHz, RT). Spectra were recorded with a 30 mT field sweep of 4096 points (94 GHz, RT), a 40 mT field sweep of 4096 points (94 GHz, 80 K), and a 60 mT field sweep of 1051 points (275 GHz, RT). The total measurement time for a recorded spectrum was 120 minutes (94 GHz, RT), 10 minutes (94 GHz, 80 K) and 8 hours (275 GHz, RT). The measurement of Cc-SL at 275

GHz was done by Peter Gast (Molecular Nano-Optics and Spins group at Leiden Institute of Physics).

Equations to calculate K_D from the fraction of bound complex c

Complex formation and dissociation are described by the equilibrium reaction



where L and P are the complex partners. The dissociation constant K_D is defined as

$$K_D = \frac{[L][P]}{[LP]}, \quad (3.2)$$

where $[L]$ is the concentration of L . Equation 3.2 is rewritten using the total concentrations $[L]_0$ and $[P]_0$:

$$K_D = \frac{(1-c)[L]_0 ([P]_0 - c[L]_0)}{c[L]_0}, \quad (3.3)$$

where c is the fraction of L that is bound to P . In the case that c is unknown, equation 3.3 is more conveniently written as

$$c = 0.5[L]_0^{-1} \left\{ K_D + [L]_0 + [P]_0 - \sqrt{K_D^2 + 2K_D([L]_0 + [P]_0) + ([L]_0 - [P]_0)^2} \right\}. \quad (3.4)$$

Principal component analysis

Principal component analysis (PCA) is used to decompose a set of spectra into linearly uncorrelated components [22] and was first applied to EPR spectra by Steinbock *et al.*^[15]. To apply PCA to the X-band EPR spectra in this work, a script was created in MATLAB (The Mathworks, Natick, MA, USA), which carries out a procedure that is identical to the one given in reference [15]. A set of n experimental EPR spectra are integrated to obtain the corresponding absorption spectra. The spectra are then normalized and imported into the script as vectors, $\bar{E}_i = \bar{E}_1, \bar{E}_2, \bar{E}_3, \dots, \bar{E}_n$. Any negative values that are due to noise are set to zero. The vectors, each consisting of m points, are stacked to form matrix C consisting of n rows and m columns. Next, matrix M is obtained by

$$M = C^T C. \quad (3.5)$$

Diagonalization of M is achieved with the MATLAB function $[V, D] = \text{eig}(M)$. The diagonal matrix D contains the eigenvalues $\lambda_j = \lambda_\alpha, \lambda_\beta, \lambda_\gamma, \dots, \lambda_m$, which are associated with the orthonormal eigenvectors $\bar{V}_j = \bar{V}_\alpha, \bar{V}_\beta, \bar{V}_\gamma, \dots, \bar{V}_m$, respectively, contained in V . The eigenvalues are sorted in order of decreasing magnitude so that λ_α has the largest value, λ_β has the second largest value, etc. A non-zero eigenvalue is significant and associated with an eigenvector that is a principal component of the spectrum. Eigenvalues that are zero are associated with eigenvectors that contain only noise. The PCA components can be used in linear combination to reconstruct any of the experimental spectra:

$$\bar{E}_i = \sum_j c_{ij} \bar{V}_j. \quad (3.6)$$

For the normalized eigenvectors \vec{V}_j

$$c_{ij} = \vec{E}_i \cdot \vec{V}_j. \quad (3.7)$$

For a two component system, i.e., only λ_α and λ_β are non-zero, the two coefficients are linearly dependant:

$$c_{i\beta} = ac_{i\alpha} + b. \quad (3.8)$$

Along this line, any spectrum $\vec{\Omega}_k$ can be constructed from the eigenvectors \vec{V}_α and \vec{V}_β for the points $(c_{k\alpha}, c_{k\beta})$ on the line defined by equation 3.8:

$$\vec{\Omega}_k = c_{k\alpha} \vec{V}_\alpha + c_{k\beta} \vec{V}_\beta. \quad (3.9)$$

The spectra of the pure components correspond to separate points located on the line defined by equation 3.8. Criteria to determine the location of these points have been described in reference [15].

Experimentally measured spectra are decomposed into ‘fraction bound’ and ‘fraction free’ by first locating their position, subsequently referred to as ‘point’, on the line defined by equation 3.9. The difference between the coordinates of the point that defines the position of the experimental spectrum and the point that defines the totally bound spectrum divided by the separation of the fully bound to the fully free spectrum is the ‘fraction of bound spectrum’ present in the experimental spectrum. For the fraction of the free protein the equivalent procedure is used, only then with respect to the point of the free spectrum.

Linear decomposition

The experimental spectrum \bar{E} is composed of the free spectrum \bar{F} and the bound spectrum \bar{B}

$$\bar{E} = f\bar{F} + b\bar{B}, \quad (3.10)$$

where f is the fraction of Cc-SL that is free and b is the fraction bound, i.e., Cc-SL in complex with CcP. Thus, we can use equation 3.10 to obtain the bound spectrum from the experimental spectrum. For this procedure, the EPR spectra are required to be normalized and superimposed such that the central lines overlap.

Simulation of EPR spectra

The cw-EPR spectra were simulated with EasySpin^[23], a software package for MATLAB (The Mathworks, Natick, MA, USA). We manually adjusted the parameters to maximize the similarity between the simulated and the experimental spectrum.

The algorithm *Pepper* was used for the simulation of the W-band spectrum of free Cc-SL in frozen solution, recorded at 80 K. From this simulation the following spin parameters were obtained: $\bar{A}_N = [A_{xx} \ A_{yy} \ A_{zz}] = [16.0 \ 15.0 \ 104.1]$ MHz, $\bar{g} = [g_{xx} \ g_{yy} \ g_{zz}] = [2.0088 \ 2.0066 \ 2.0028]$. These values were then used for all other simulations.

The algorithm *Garlic* was used for the solution spectra recorded at room temperature. This algorithm allows for the adjustment of the rotation-correlation time, $\tau_r = [\tau_{xx} \ \tau_{yy} \ \tau_{zz}]$. We found that the solution spectra are best simulated with two components – one component that represents a fast mobility, the other a slow mobility. We used two restrictions in our approach to

simulate the spectra of free Cc-SL: i) the τ_r and the ratio of two components were taken equal for the spectra in X-band and W-band; ii) the fast and slow component were given an anisotropic and isotropic rotation, respectively. The same approach was used in the simulation of the X-band and W-band spectra of bound Cc-SL.

The protein rotation-correlation time

For a globular protein with radius r , the rotation-correlation time is calculated using the Stokes-Einstein relation

$$\tau_r = \frac{4\pi r^3 \eta}{3k_B T}, \quad (3.11)$$

where η is the viscosity of water (1.00 mP·s), k_B the Boltzmann constant, and T is the temperature, in this work: 293 ± 1 K. We used distance measurements in the crystal structure of Cc:CcP (PDB entry 2PCC^[24]) to estimate the radius of Cc and that of the complex. A hydration radius of 0.24 nm was taken into account.

Calculation with HYDRONMR^[25] based on PDB entry 2PCC^[24] was used as an alternative route to calculate the isotropic τ_r of Cc and the complex.

3.3 Results

Figure 3.2 shows a series of X-band EPR spectra of spin-labelled cytochrome *c* (Cc-SL) measured in the presence of increasing concentrations of cytochrome *c* peroxidase (CcP). The spectrum in Figure 3.2a is that of free Cc-SL and shows three lines. With CcP added, additional features appear (indicated by arrows in Figure 3.2b to g). With increasing CcP concentration, the intensity of these features increases and the signal intensity of free Cc-SL decreases. A control experiment with Cc-SL in a 1:3 ratio with CcP at high salt concentration is shown in yellow in Figure 3.2a. This spectrum is identical to that of free Cc-SL, indicating that a high ionic strength prevents complex formation.

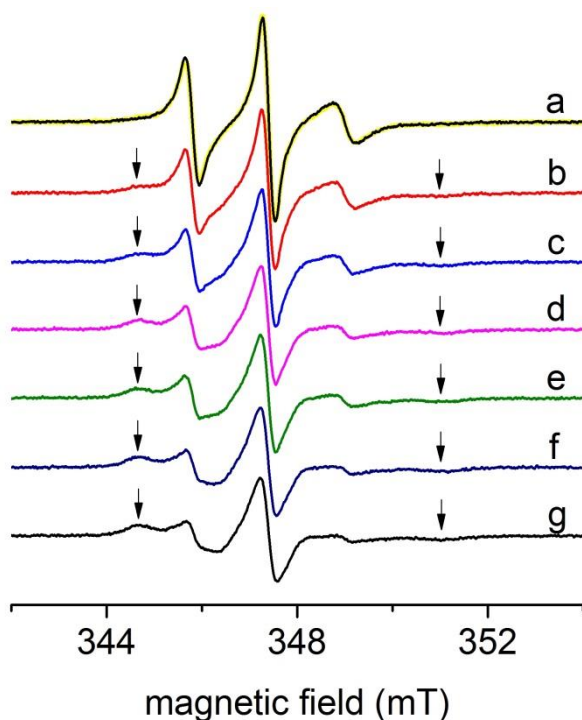


Figure 3.2 The X-band room-temperature EPR spectra of spin-labelled cytochrome *c* (Cc-SL) with different concentrations of CcP added. (a) 100 μM Cc-SL without CcP, (b) 100 μM with 50 μM CcP, (c) with 75 μM CcP, (d) with 100 μM CcP, (e) with 133 μM CcP, (f) with 200 μM CcP, and (g) with 400 μM CcP. The arrows indicate lines in spectra (b) to (g) that are not present in spectrum (a). Spectrum (a) is overlaid with the spectrum of 135 μM Cc-SL, 388 μM CcP with 556 mM NaCl (in yellow).

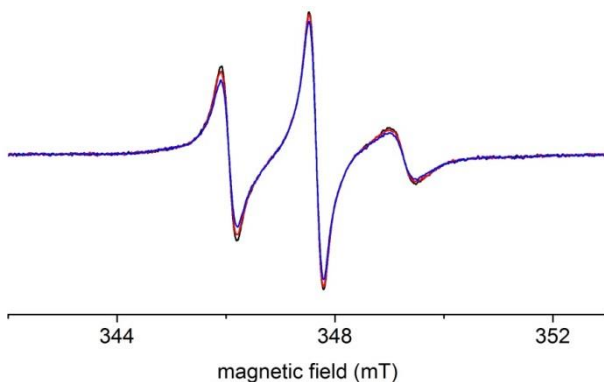


Figure 3.3 The X-band room-temperature EPR spectra of Cc-SL with bovine serum albumin (BSA). In black: 161 μM Cc-SL; in red: 161 μM Cc-SL with 161 μM BSA; in blue: 161 μM Cc-SL with 430 μM BSA.

In Figure 3.3, the X-band EPR spectra are shown of Cc-SL measured with bovine serum albumin (BSA), a protein that should not bind Cc specifically and is therefore suitable as a control. The figure shows the spectrum of Cc-SL alone, in 1:1 and 1:2.7 mixture with BSA. The three spectra are not identical; with increasing concentration of BSA a subtle line broadening is detected compared to the spectrum of Cc-SL alone, suggesting a very weak, non-specific interaction between the proteins. Nonetheless, the spectral changes detected in the spectra of Cc-SL with BSA are much smaller than in spectra of samples in which CcP is added (Figure 3.2).

Figure 3.4 shows the W-band EPR spectra of Cc-SL measured with different concentrations of CcP. With CcP added, features are visible (indicated by arrows in Figure 3.4b to d) that correspond to a signal with broader lines than the free Cc-SL (Figure 3.4a), particularly in the high-field region. In Figure 3.4a and b the asterisks indicate a background signal that was also encountered when an empty quartz capillary is measured (data not shown). The asterisks in Figure 3.4c indicate the sharp lines that likely originate from a manganese impurity.

The frozen-solution spectra of Cc-SL (Figure 3.4e) and Cc-SL:CcP 1:1 (Figure 3.4f) have singularities at identical field positions revealing that the \bar{g}

and $\bar{\bar{A}}_N$ parameters of free *Cc*-SL and the bound form do not differ significantly in the frozen state. Therefore, $\bar{\bar{g}}$ and $\bar{\bar{A}}_N$ parameters for the simulation of the solution spectra were derived from the simulation of the spectrum in Figure 3.4e.

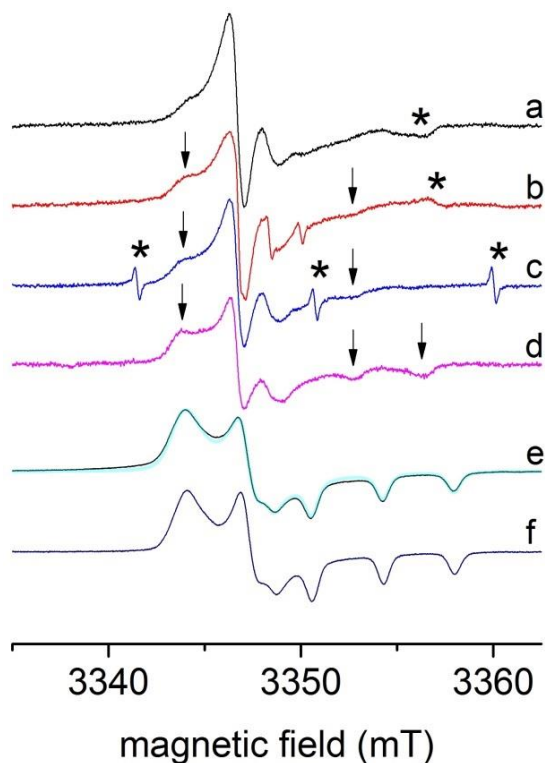


Figure 3.4 The W-band EPR spectra of *Cc*-SL with different concentrations of CcP at room temperature (RT) and at 80 K. 400 μM *Cc*-SL (a) without CcP (RT), (b) with 100 μM CcP (RT), (c) with 200 μM CcP (RT), (d) 414 μM *Cc*-SL with 400 μM CcP (RT), (e) 482 μM *Cc*-SL without CcP (80 K), and (f) 371 μM *Cc*-SL with 373 μM CcP (80 K). In the room-temperature spectra, the arrows indicate lines that are more pronounced than in the spectrum shown in (a). The asterisk in (a) and (b) indicates a background signal. The asterisks in (c) indicate sharp lines that likely originate from a manganese impurity. The spectrum of free *Cc*-SL recorded at 80 K, shown in (e), was used for simulation (in cyan) to obtain the tensors $\bar{\bar{g}}$ and $\bar{\bar{A}}_N$ given in Material and Methods.

Figure 3.5 displays the room-temperature EPR spectrum of free *Cc*-SL recorded at 275 GHz. A sharp line, indicated by an asterisk, is attributed to a manganese impurity. The spectrum spreads over 50 mT, whereas the W-band spectrum has a spread of less than 20 mT, showing the higher resolving power of 275 GHz EPR. The 275 GHz spectrum has features at the field values marked g_{xx} , g_{yy} and a broad, low intensity band around the field value marked g_{zz} .

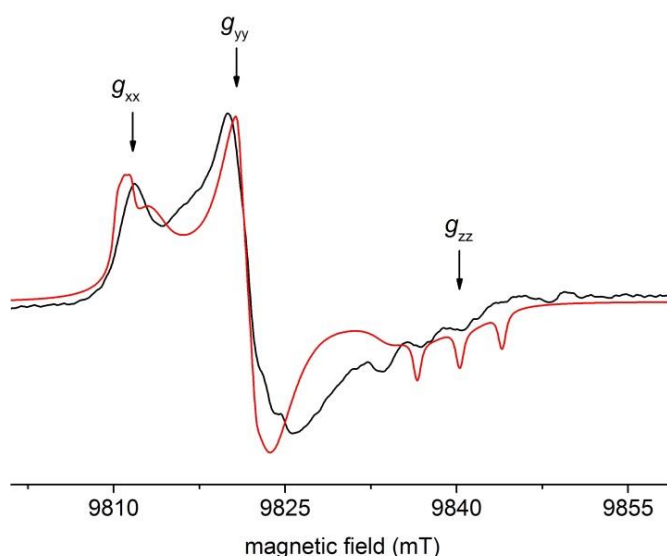


Figure 3.5 The room-temperature EPR spectrum of free *Cc*-SL recorded at 275 GHz. The experimental spectrum (shown in black) contains an underlying powder spectrum, which is revealed by the pronounced feature at g_{xx} . A mix of a solution spectrum (70%) and a powder spectrum (30%) was used to obtain the simulation (shown in red). We used the g and A_N tensor values as given in Material and methods. Furthermore, we used the rotation-correlation times and fraction ratios of the free *Cc*-SL (see Table 3.1) and a combination of a Gaussian and Lorentzian lineshape (0.2 mT and 0.4 mT linewidth, respectively). The powder spectrum was obtained with the algorithm *Pepper*.

The PCA analysis of the X-band EPR spectra from Figure 3.2 yielded two eigenvalues that were non-zero: $\lambda_\alpha = 1.875$ and $\lambda_\beta = 0.019$. Consequently, the

EPR spectra derive from a two-component system. Figure 3.6 shows the result of the PCA analysis on the X-band spectra. The values for $c_{i\alpha}$ and $c_{i\beta}$, obtained from equation 3.7, are plotted in Figure 3.6a. A linear fit through the points yields the relation

$$c_{i\beta} = 1.55 - 3.00 c_{i\alpha} . \quad (3.12)$$

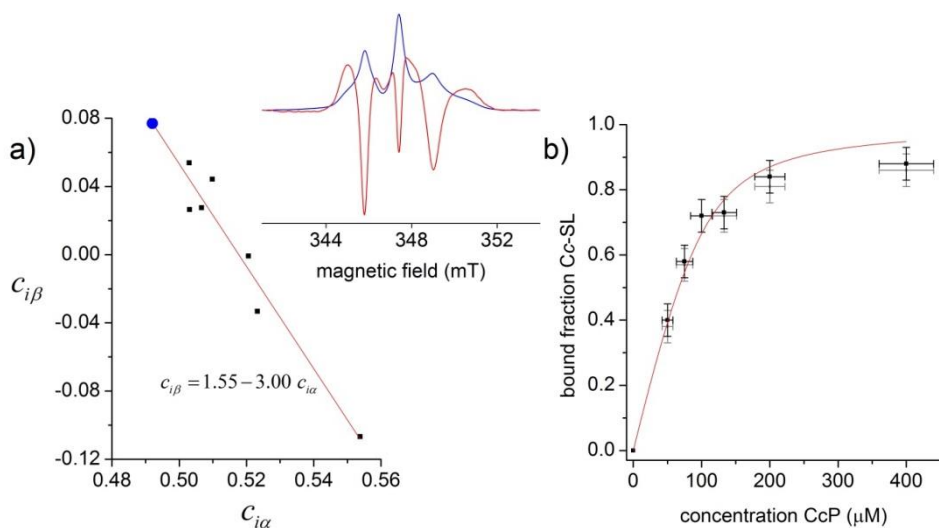


Figure 3.6 Result of the PCA analysis of the X-band spectra of Cc-SL:CcP (see Figure 3.2). a) Black dots: $(c_{i\alpha}, c_{i\beta})$ points of the experimental spectra. The trend line (in red) is obtained by a linear fit through the seven points. The blue dot marks the position of the fully bound spectrum, point $(c_{i\alpha}, c_{i\beta}) = (0.491, 0.077)$. Inset: eigenvectors \bar{v}_α (in blue) and \bar{v}_β (in red). b) The bound fractions of Cc-SL versus the concentration of CcP in the seven X-band EPR measurements obtained by PCA (in black) and obtained by linear decomposition (in grey). The horizontal error bars represent the uncertainty in the CcP concentrations due to multiple dilution steps in the preparation of the EPR samples. The vertical error bars represent the uncertainty in determining the fraction of bound Cc-SL and is mainly caused by the noise level in the EPR spectra. The dissociation constant, $K_d = 17 \pm 3 \mu\text{M}$, was determined by a fit (red line) with equation 3.4.

The eigenvectors \vec{V}_α and \vec{V}_β that resulted from the PCA analysis are shown as an inset in Figure 3.6a. With these eigenvectors and equations 3.9 and 3.12, several spectra were inspected in the range $0.480 \leq c_{i\alpha} \leq 0.500$ to determine the bound spectrum. The spectrum selected as the most bound spectrum is shown in Figure 3.7c. This point is $(c_{i\alpha}, c_{i\beta}) = (0.491, 0.077)$ and is shown in Figure 3.6a as a blue dot. From the PCA analysis, the fraction of bound Cc-SL (b) for each measurement was determined by the following equation:

$$b = \frac{c_{i\beta}(\text{measurement}) - c_{i\beta}(\text{free})}{c_{i\beta}(\text{bound}) - c_{i\beta}(\text{free})}. \quad (3.13)$$

To determine K_D , in Figure 3.6b the fraction of bound Cc-SL derived from the PCA analysis is plotted versus the concentration of CcP in the seven measurements (see Figure 3.2). The dissociation constant that best fits this data (equation 3.4) is $K_D = 17 \pm 3 \mu\text{M}$.

Linear decomposition resulted in a K_D that is identical within the error margins. The W-band EPR spectra showed four principal components in PCA, rather than the two components expected from the results of the X-band EPR spectra. We attribute the additional components to spurious signals and baseline instabilities, which are more pronounced in the W-band than in the X-band EPR spectra, and therefore abandoned PCA on the W-band EPR spectra.

Analysis by linear decomposition works better. To extract the fully bound spectrum, a fraction of the free spectrum of Cc-SL (Figure 3.4a) was subtracted from the spectrum in Figure 3.4d. The amount of free spectrum was varied in the range of 10% to 50% and the value of 20% was selected by visual inspection resulting in the spectrum shown in Figure 3.7d.

Rotation-correlation times of the spin label were determined by simulations of the spectra of free Cc-SL and of Cc-SL fully bound to CcP (Cc-SL:CcP, Figure 3.7). To satisfactorily simulate the X-band and the W-band spectra, two components were used, one of which had a rhombic rotation tensor. Models including an ordering potential^[26] were not tried. In free Cc-SL, a majority fraction (60%) of the spin label rotates with a τ_r that is anisotropic and overall smaller than the τ_r of the protein (Table 3.1). The second fraction is isotropic and has a τ_r close to that of the protein. The simulation parameters are also compatible with the 275 GHz EPR spectrum of free Cc-SL (Figure 3.5).

Table 3.1 The parameters used for the simulation of cw-EPR spectra of spin-labelled cytochrome *c* alone (free) and in complex with cytochrome *c* peroxidase (bound).

state of Cc-SL	fast component ^a					slow component ^a		protein/complex	
	τ_{xx} (ns)	τ_{yy} (ns)	τ_{zz} (ns)	isotropic τ_r (ns)	fraction	isotropic τ_r (ns)	fraction	isotropic τ_r (ns)	
free	2	0.7	3	1.3	60%	5	40%	5.6 ^b	7.3 ^c
bound	8	1.5	8	3.3	20%	8	80%	18.5 ^b	29 ^c

^a The spectral lines were described with a Gaussian (g) and/or Lorentzian (l) lineshape. The linewidths used were: X-band free: 0.03 mT (g), 0.04 mT (l) / W-band free: 0.3 mT (l) / X-band bound: 0.07 mT (g)/ W-band bound: 0.1 mT (l).

^b The values were calculated with equation 3.11.

^c The values were calculated with HYDRONMR^[25] (see Material and Methods).

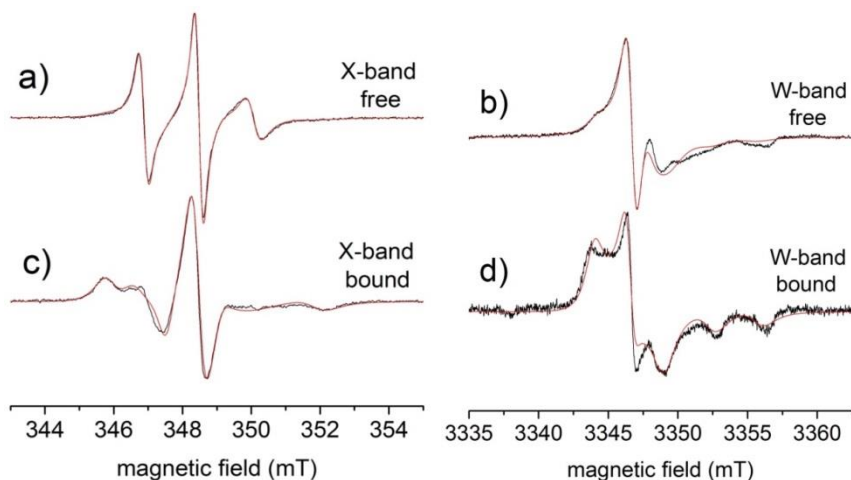


Figure 3.7 The free and bound spectra of Cc-SL in solution at X-band and W-band. The experimental and simulated data are shown in black and red, respectively. The experimental data in a) and b) are spectra directly obtained from measurement. The experimental data in c) was obtained via PCA (see Material and methods) applied to the spectra shown in Figure 3.2. The experimental data in d) was obtained via linear decomposition (see Material and methods) of the spectra shown in Figures 3.4a and d. The simulations were obtained with the parameters listed in Table 3.1. Note: for the spectra in a) and c) an up-field shift of 1.1 mT was applied compared to the spectra in Figure 3.2.

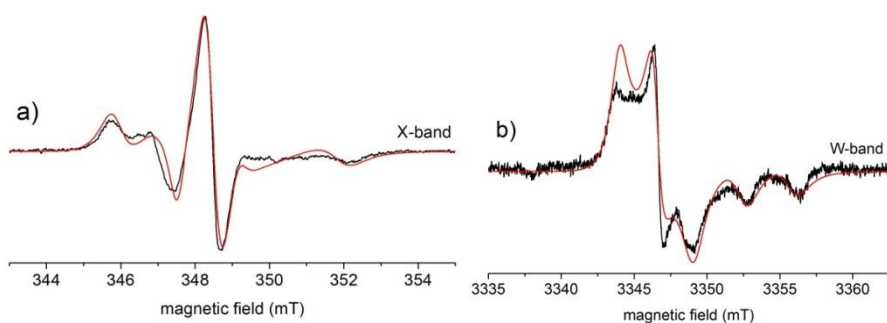


Figure 3.8 Simulations of the fully bound spectrum showing the effect of the fast component on the spectra. Simulations (red) of X-band (a) and W-band (b) spectrum without the fast component, i.e., using only an isotropic rotation-correlation time of 8 ns. The experimental spectra are identical to the spectra in Figures 3.7c and d.

In the fully-bound state, the rotation is slower than for free Cc-SL. The larger fraction (80%) has an isotropic rotation with a τ_r of 8 ns, and the smaller fraction has an anisotropic rotation, with an average τ_r that is about twice as long as that of the fast fraction in the free Cc-SL. The anisotropic rotation has the smallest component along the y -axis of the nitroxide in the simulations of both spectra. Simulation parameters may not be unique, and, in particular, several solutions for the anisotropy of the rotation were found, which agree with the data. Figure 3.8 shows the same experimental spectra as in Figures 3.7c and d and simulations of the spectra, which were obtained with an isotropic τ_r of 8 ns, i.e., in which for the smaller, fast component in Table 3.1 is omitted. The simulations in Figures 3.8a and b agree less with the experimental spectra than in Figures 3.7c and d, which illustrates that the smaller fraction is essential for a satisfactory interpretation of the bound spectra.

The parameter set given in Table 3.1 fits best to the X- and the W-band spectra simultaneously. We have not systematically investigated whether there are correlations between different simulation parameters, e.g. the contribution of components and τ_r , such as described earlier^[26]. The overall rotation of the free Cc-SL is faster than for Cc-SL in the complex with CcP.

3.4 Discussion

We show an approach to locally map the environment at the interface of a transient complex. To do so, a set of EPR spectra of samples with different ratios of complex-binding partners has been analysed. The fully overlapping spectra were disentangled to obtain K_D and the spectra of the free and fully bound states. We employ the sensitivity of multi-frequency EPR to nanosecond motion of a spin label and determine the change in the rotation-correlation time of the spin label as the complex is formed.

Systematic changes in motion of the spin label attached to Cc (Cc-SL) occur, when Cc-SL is in the presence of the complex-binding partner (CcP), Figures 3.2 and 3.4. At salt concentrations known to disrupt the complex, these changes disappear (Figure 3.2a). The spectral changes, therefore, are due to complex formation and not caused by an increase of the solution viscosity due to the presence of the complex partner. The small spectral changes observed when adding BSA, a protein we used as a negative control (Figure 3.3), must be due to unspecific binding. Having thus established that the spectra monitor complex formation, we proceed to further characterize the spectra.

To map the change in spin-label motion in the free and fully bound state of Cc-SL, spectral analysis is performed. Particularly, the spectrum of Cc-SL in complex with CcP needs attention, because mixtures of Cc-SL and CcP always contain a fraction of free Cc-SL, even at a large excess of CcP. A contribution of free Cc-SL in the order of 5% remains and since the spectrum of free Cc-SL has narrower lines than that of Cc-SL in complex with CcP (see below), the free Cc-SL contribution disturbs the lineshape. We used PCA and linear decomposition to determine the EPR spectrum of bound Cc-SL and the fraction by which this spectrum contributes to the experimental spectra of mixtures of Cc-SL with different ratios of CcP. The fraction of bound Cc-SL serves to determine the K_D value (see Results). The K_D thus obtained (17 ± 3

μM) agrees well with the results of recent NMR experiments: $K_D = 19 \pm 4 \mu\text{M}$ ^[27], which were performed on the protein construct A81C linked with a diamagnetic variant of the spin label, showing that EPR and NMR monitor the same state of the complex. Spin-label dynamics of free Cc-SL and fully bound Cc-SL differ considerably. The free Cc-SL contains a large fraction of a mobile component. Since the rotation-correlation time is smaller than that of the protein, local mobility, i.e., rotation about the single bonds linking the spin label to the protein backbone is dominant in that fraction. The local motion is frozen out in the second fraction, and the nitroxide must be locked to the protein. The spin label is either completely immobilized at the protein surface, or, if it has residual motion, the correlation time of this motion must be larger than 5.6 ns, the τ_r of the protein.

When Cc-SL is in complex with CcP, the local mobility of the spin label is reduced, leading to larger τ_r values and a smaller fraction of the mobile form (20% compared to 60% in the free form). To demonstrate the validity of the interpretation of two fractions, in Fig. 3.8 we compare the fully bound spectrum with simulations in which the mobile fraction is omitted. Notably, the simulation of the X-band spectrum is still acceptable, but the W-band spectrum is not compatible with that interpretation. This demonstrates that by high-field EPR, previously inaccessible detail of complex formation can be determined. In Fig. 3.5, we show that this limit can be pushed even further. The spectrum at 275 GHz, measured on the free Cc-SL at 3 mM concentration shows that a sufficiently high signal-to-noise ratio can be achieved to perform lineshape analysis in the future.

According to NMR studies, in the wild-type Cc:CcP about 30% of the complex is in the dynamic, encounter state, while the rest is in the productive, specific complex, suitable for electron transfer^[10]. One could speculate that the

20% fraction observed by EPR is due to proteins in the encounter complex, whereas the slower fraction is the protein in the stereo-specific complex. Under these assumptions, the spin label in the stereo-specific complex would be pinned to the interaction surface of both proteins. Residual mobility could still be present, because the τ_r of this fraction is smaller than the τ_r calculated for the protein complex. Consequently, the more mobile fraction would be due to the encounter complex and the spin-label mobility would reflect the dynamics and local structure of the encounter complex. In our simulations, the additional mobility component manifests itself in a faster rotation about the spin-label g_{yy} -axis (see Figure 1.2), suggesting that in the encounter complex the spin label is more free to rotate about this axis. Additional simulations are needed to prove this anisotropic rotation model, simulations that would be aided by 275 GHz experiments to be performed in the future.

Immobilization upon complex formation has been found before for the complex of *Cc* with cytochrome *bc_1* by Sarewicz et al.^[28]. Novel in the present study is the possibility to discriminate between two fractions in the EPR spectra, potentially related to the encounter and the stereospecific complex (fast and mobile fractions).

References

- [1] M. Ubink, The courtship of proteins: Understanding the encounter complex. *Febs Letters* **583** (2009) 1060-1066.
- [2] Y.C. Kim, C. Tang, G.M. Clore, G. Hummer, Replica exchange simulations of transient encounter complexes in protein-protein association. *Proceedings of the National Academy of Sciences of the United States of America* **105** (2008) 12855-12860.
- [3] A.N. Volkov, J.A.R. Worrall, E. Holtzmann, M. Ubink, Solution structure and dynamics of the complex between cytochrome c and cytochrome c peroxidase determined by paramagnetic NMR. *Proceedings of the National Academy of Sciences of the United States of America* **103** (2006) 18945-18950.
- [4] M. Prudencio, M. Ubink, Transient complexes of redox proteins: structural and dynamic details from NMR studies. *Journal of Molecular Recognition* **17** (2004) 524-539.
- [5] J. Schilder, M. Ubink, Formation of transient protein complexes. *Current Opinion in Structural Biology* **23** (2013) 911-918.
- [6] T. Selzer, G. Schreiber, New insights into the mechanism of protein-protein association. *Proteins-Structure Function and Genetics* **45** (2001) 190-198.
- [7] F.B. Sheinerman, R. Norel, B. Honig, Electrostatic aspects of protein-protein interactions. *Current Opinion in Structural Biology* **10** (2000) 153-159.
- [8] I. Diaz-Moreno, A. Diaz-Quintana, M.A. De la Rosa, M. Ubink, Structure of the complex between plastocyanin and cytochrome f from the cyanobacterium *Nostoc* sp PCC 7119 as determined by paramagnetic NMR - The balance between electrostatic and hydrophobic interactions within the transient complex determines the relative orientation of the two proteins. *Journal of Biological Chemistry* **280** (2005) 18908-18915.
- [9] R. Hulsker, M.V. Baranova, G.S. Bullerjahn, M. Ubink, Dynamics in the transient complex of plastocyanin-cytochrome f from *Prochlorothrix hollandica*. *Journal of the American Chemical Society* **130** (2008) 1985-1991.
- [10] Q. Bashir, A.N. Volkov, G.M. Ullmann, M. Ubink, Visualization of the Encounter Ensemble of the Transient Electron Transfer Complex of Cytochrome c and Cytochrome c Peroxidase. *Journal of the American Chemical Society* **132** (2010) 241-247.
- [11] A.N. Volkov, Transient Complexes of Heme Proteins, dissertation, Leiden University (2007).
- [12] V.P. Timofeev, V.V. Novikov, Y.V. Tkachev, T.G. Balandin, A.A. Makarov, S.M. Deyev, Spin label method reveals barnase-barstar interaction: A temperature and viscosity dependence approach. *Journal of Biomolecular Structure & Dynamics* **25** (2008) 525-534.
- [13] M. Sarewicz, A. Borek, F. Daldal, W. Froncisz, A. Osyczka, Demonstration of short-lived complexes of cytochrome c with cytochrome bc(1) by EPR spectroscopy - Implications for the mechanism of interprotein electron transfer. *Journal of Biological Chemistry* **283** (2008) 24826-24836.

- [14] M. Sarewicz, S. Szytula, M. Dutka, A. Osyczka, W. Froncisz, Estimation of binding parameters for the protein-protein interaction using a site-directed spin labeling and EPR spectroscopy. *European Biophysics Journal with Biophysics Letters* **37** (2008) 483-493.
- [15] O. Steinbock, B. Neumann, B. Cage, J. Saltiel, S.C. Muller, N.S. Dalal, A demonstration of principal component analysis for EPR spectroscopy: Identifying pure component spectra from complex spectra. *Analytical Chemistry* **69** (1997) 3708-3713.
- [16] J. Schilder, F. Lohr, H. Schwalbe, M. Ubbink, The cytochrome c peroxidase and cytochrome c encounter complex: The other side of the story. *Febs Letters* **588** (2014) 1873-1878.
- [17] J.A.R. Worrall, U. Kolczak, G.W. Canters, M. Ubbink, Interaction of yeast iso-1-cytochrome c with cytochrome c peroxidase investigated by [N-15,H-1] heteronuclear NMR spectroscopy. *Biochemistry* **40** (2001) 7069-7076.
- [18] W.B.R. Pollock, F.I. Rosell, M.B. Twitchett, M.E. Dumont, A.G. Mauk, Bacterial expression of a mitochondrial cytochrome c. Trimethylation of Lys72 in yeast iso-1-cytochrome c and the alkaline conformational transition. *Biochemistry* **37** (1998) 6124-6131.
- [19] A.S. Morar, D. Kakouras, G.B. Young, J. Boyd, G.J. Pielak, Expression of N-15-labeled eukaryotic cytochrome c in *Escherichia coli*. *Journal of Biological Inorganic Chemistry* **4** (1999) 220-222.
- [20] H. Blok, J.A.J.M. Disselhorst, S.B. Orlinskii, J. Schmidt, A continuous-wave and pulsed electron spin resonance spectrometer operating at 275 GHz. *Journal of Magnetic Resonance* **166** (2004) 92-99.
- [21] G. Mathies, H. Blok, J.A.J.M. Disselhorst, P. Gast, H. van der Meer, D.M. Miedema, R.M. Almeida, J.J.G. Moura, W.R. Hagen, E.J.J. Groenen, Continuous-wave EPR at 275 GHz: Application to high-spin Fe³⁺ systems. *Journal of Magnetic Resonance* **210** (2011) 126-132.
- [22] K.R. Beebe, B.R. Kowalski, An Introduction to Multivariate Calibration and Analysis. *Analytical Chemistry* **59** (1987) 1007 A-1017 A.
- [23] S. Stoll, A. Schweiger, EasySpin, a comprehensive software package for spectral simulation and analysis in EPR. *Journal of Magnetic Resonance* **178** (2006) 42-55.
- [24] H. Pelletier, J. Kraut, Crystal-Structure of A Complex Between Electron-Transfer Partners, Cytochrome-C Peroxidase and Cytochrome-C. *Science* **258** (1992) 1748-1755.
- [25] J.G. de la Torre, M.L. Huertas, B. Carrasco, HYDRONMR: Prediction of NMR relaxation of globular proteins from atomic-level structures and hydrodynamic calculations. *Journal of Magnetic Resonance* **147** (2000) 138-146.
- [26] D.E. Budil, S. Lee, S. Saxena, J.H. Freed, Nonlinear-least-squares analysis of slow-motion EPR spectra in one and two dimensions using a modified Levenberg-Marquardt algorithm. *Journal of Magnetic Resonance Series A* **120** (1996) 155-189.
- [27] J. Schilder, *et al.*, *work to be published*.
- [28] M. Sarewicz, A. Borek, F. Daldal, W. Froncisz, A. Osyczka, Estimation of the lifetime of the complex between cytochrome c and cytochrome bc(1) using electron paramagnetic resonance. *Biochimica et Biophysica Acta-Bioenergetics* **1777** (2008) S103.

4

SPIN-SPIN INTERACTION IN RIGID 3_{10} -HELICAL PEPTIDES WITH TOAC SPIN LABELS: AN EPR POWER-SATURATION STUDY

4.1 Introduction

Electron paramagnetic resonance has become a powerful technique in biological structure determination. Most commonly, structure determination relies on measuring distances between paramagnetic centres, often spin labels, attached to specific positions in the biomacromolecules of interest. The most powerful techniques to measure such distances by EPR are limited in two aspects: they work for frozen solutions at low temperatures^[1;2] and distance ranges between 0.8 – 1.5 nm are difficult to address^[3]. Physiological conditions, such as liquid solutions at room temperature, pose additional challenges. The dipolar interaction between spins, so far the most reliable indicator for distance, can be partially averaged in liquid solution, and the isotropic exchange interaction J is a short-range interaction (several tenths of nanometres) and is difficult to interpret in terms of distance between spins. Also, in liquid solution, the spin-spin interaction is extracted from lineshape. Particularly, the difference in the spectra of the system of interest in the absence and the presence of the spin-spin interaction is evaluated, and therefore small spin-spin interactions and longer distances are difficult to measure. Here we show that for nitroxides, in the distance regime of 0.8 – 1.5 nm electron

spin-spin relaxation could be used as an indicator for distance, expanding the tools available to EPR so far even further towards biologically relevant conditions.

In this study, we determine the relaxation parameters by power-saturation experiments. We investigate a series of four rigid bi-radical peptides and corresponding size-matched mono-radical peptides described before^[4]. The peptides consist of the non-coded, host α -amino acid α -aminoisobutyric acid (Aib), combined with one or two 4-amino-1-oxy-2,2,6,6-tetramethyl-piperidine-4-carboxylic acid (TOAC) guest residues. The series consists of the bi-radicals HEPTA_{3,6}, HEXA_{1,5}, OCTA_{2,7}, NONA_{2,8}, and the mono-radicals HEPTA₆, OCTA₇, NONA₂, where the subscript indicates the TOAC positions. Exact sequences are given in Table 1 in reference [4]. In the previous study, the peptides were classified according to the magnitude of the exchange interaction: HEPTA_{3,6} and HEXA_{1,5} with a large exchange interaction and five-line EPR spectra as class I and OCTA_{2,7} and NONA_{2,8}, with a small exchange interaction and three-line EPR spectra, as class II^[4].

We demonstrate that in all cases the relaxation parameters of the bi-radicals differ significantly from the mono-radicals, showing that an additional relaxation mechanism operates in the bi-radicals. We attribute the additional relaxation to the spin-spin interaction in the bi-radicals and posit that it could be used as a tool for distance determination.

4.2 Material and methods

The synthesis of the peptides has been described previously, for NONA₉ and NONA_{2,8} in reference [5], for HEPTA_{3,6} in reference [6], for HEPTA₆, HEXA_{1,5}, OCTA_{2,7}, and OCTA₇ in reference [4]. The details about the sample preparation of the peptides are given in reference [4].

EPR measurements

The series of microwave-power saturation experiments were done at 9.7 GHz using an ELEXSYS E 680 spectrometer (Bruker BioSpin GmbH, Rheinstetten, Germany) equipped with a dielectric cavity. The peptides were measured over a range of 0.2 W to 0.2 mW of microwave power, in steps of 1dB attenuation. The measurements were done with a field sweep of 15 mT, 2048 field points, a time constant of 5.12 ms, and a conversion time of 5.12 ms. The modulation frequency was 100 kHz. The modulation amplitude was 0.05 mT for HEXA_{1,5}, 0.10 mT for HEPTA_{3,6}, and 0.03 mT for the other peptides. Only one scan was needed per level of power attenuation, except for the peptides HEXA_{1,5} and HEPTA_{3,6}, for which up to 36 scans per level of power attenuation were done to increase the signal-to-noise ratio. To monitor the temperature in the dielectric cavity, a chromel/alumel thermocouple with a readability of 0.1 K was used. A constant stream of N₂ was sent through the cavity to maintain a temperature of 293 K.

Theoretical aspects

A saturation curve is obtained in cw mode by measuring the amplitude Y of a first-derivative EPR line (see Figure 4.1) as a function of the microwave power P . The shape of the saturation curve is, amongst others, determined by the product $T_1 T_2$ [7]

$$Y \propto \frac{B_1}{(1 + B_1^2 \gamma^2 T_1 T_2)^\varepsilon} \quad (4.1)$$

where B_1 is the microwave magnetic field, $\gamma = g_e \mu_B / \hbar$, and ε is a measure for the homogeneity of the saturation. For a homogeneously broadened (Lorentzian) line, $\varepsilon = 1.5$. For an inhomogeneously broadened (Gaussian) line, $\varepsilon = 0.5$. In order to determine $T_1 T_2$ from the saturation curve, the amplitudes are fitted to^[8]

$$Y = \frac{I \sqrt{P}}{\left[1 + (2^{1/\varepsilon} - 1) P / P_{1/2} \right]^\varepsilon}, \quad (4.2)$$

where I is a scaling factor. The combination of equations 4.1 and 4.2 gives

$$P_{1/2} = \frac{2^{1/\varepsilon} - 1}{\Lambda^2 \gamma^2 T_1 T_2}, \quad (4.3)$$

where Λ is the resonator efficiency^[9]

$$\Lambda = \frac{B_1}{\sqrt{P}}. \quad (4.4)$$

4.3 Results

The cw spectra of peptides OCTA₇ and HEPTA_{3,6} are shown in Figure 4.1 and are representative for three-line spectra of class II and five-line spectra of class I peptides, respectively. The lines are referred to with $m_i = +1, 0, -1$ and $M_i = +2, +1, 0, -1, -2$. The cw-EPR spectra of all peptides in this study are shown and analysed in reference [4]. For power saturation measurements, the complete spectra were measured at 31 power settings. Care was taken to measure each compound under comparable conditions (see Material and methods). The line intensities were obtained as shown by the red arrows in Figure 4.1 and plotted as a function of \sqrt{P} (Figure 4.2).

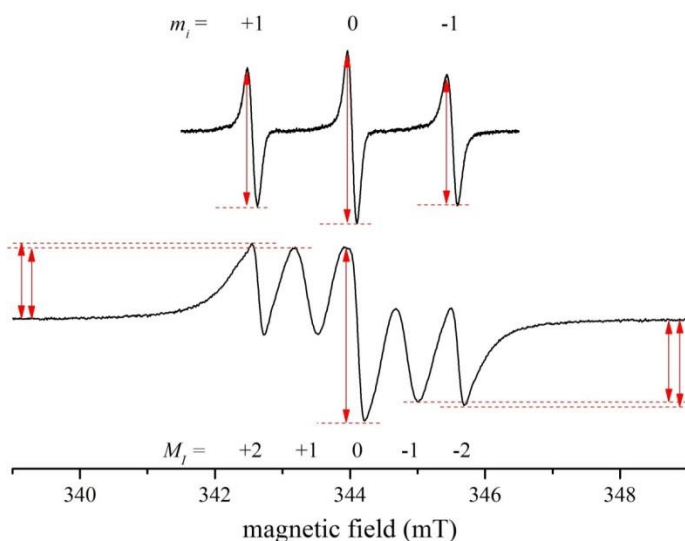


Figure 4.1 Typical cw-EPR spectra of the peptides investigated here. The top spectrum, of OCTA₇, is typical for mono-radicals and class II bi-radicals (conditions: one scan at 63.3 mW). The bottom spectrum, of HEPTA_{3,6}, is typical for class I bi-radicals (conditions: 25 scans accumulated at 25.2 mW). The indexes $m_i = +1, 0, -1$ and $M_i = +2, +1, 0, -1, -2$ are used to refer to the three and five spectral lines, respectively. The red arrows show how the first-derivative amplitudes of the spectral lines were measured in the respective spectra.

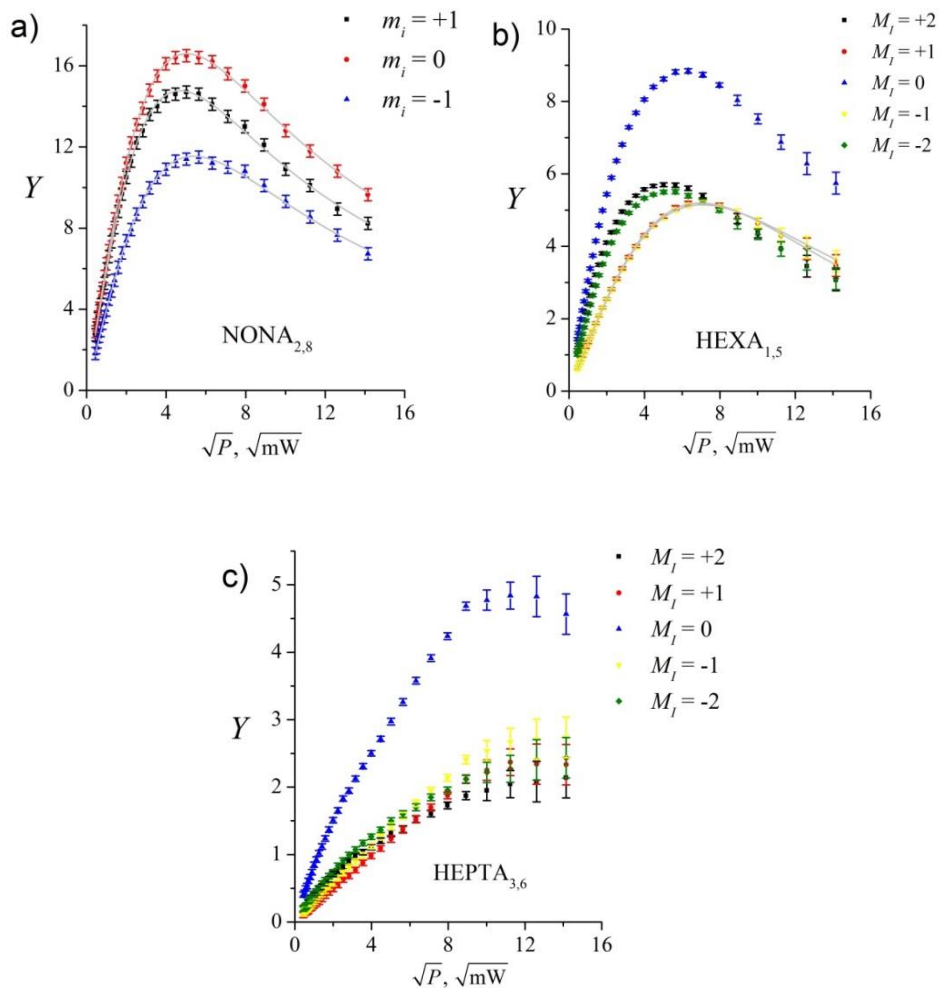


Figure 4.2 Examples of saturation curves for mono-radical and class I peptides (NONA_{2,8}) and the two class II peptides (HEXA_{1,5} and HEPTA_{3,6}) with the first-derivative amplitudes plotted against \sqrt{P} . Note that because of the definition of the amplitude (Figure 4.1), the amplitude of the $M_l = 0$ component is twice that of the remaining components. For each amplitude, the error bar is taken as twice the amplitude of the noise. The saturation curves that could be fitted to equation 4.2 are shown as grey lines.

The fits according to equation 4.2 (shown in Figure 4.2 as grey lines) yield the characteristic powers of half-saturation ($P_{1/2}$) and parameters ε , which are listed in Table 4.1. The powers $P_{1/2}$, which we discuss first, reflect the ease of saturation. For peptides NONA₉, NONA_{2,8}, HEPTA₆, OCTA_{2,7}, and OCTA₇, $P_{1/2}$ increases in the order of decreasing m_i , similar to the trend in increasing linewidths^[4]. In the saturation curves for the HEXA_{1,5} (Figure 4.2b), the $M_I = \pm 2$ and 0 components saturate differently than the $M_I = \pm 1$ components. The initial linear part of the curve is steeper, for $M_I = \pm 2$ and 0, and the maximum of the amplitude is reached at lower powers than for the $M_I = \pm 1$ component. The saturation behaviour of the $M_I = \pm 1$ component is fitted by equation 4.2, yielding the parameters given in Table 4.1. For the $M_I = \pm 2$ and 0 components the curves cannot be fitted with meaningful values. Also, fitting with two components did not yield unique solutions. Therefore, only values for the $M_I = \pm 1$ components can be determined. Also, for this peptide no significant difference is observed between the $P_{1/2}$ values of the $M_I = \pm 1$ and $M_I = -1$ lines. For peptide HEPTA_{3,6}, the maximally available power of the instrument was not sufficient to reach full saturation (Figure 4.2c), therefore only a lower limit for $P_{1/2}$ can be determined: $P_{1/2} > 200$ mW.

The ε values, which reflect whether the line is Lorentzian ($\varepsilon = 1.5$) or Gaussian ($\varepsilon = 0.5$), for most compounds are in the range for mixtures of these two fundamental lineshapes, showing that the lines are partially inhomogeneously broadened, presumably on account of hyperfine broadening. Only HEXA_{1,5} has an ε value ($\varepsilon = 1.5$) appropriate for a purely Lorentzian line, showing that the lineshape for this bi-radical is determined by a process,

which is so fast that it dominates the lineshape. For none of the compounds a purely Gaussian saturation behaviour ($\varepsilon = 0.5$) is seen.

Table 4.1 Relaxation parameters of mono- and bi-radical peptides.

		$m_i = +1$		$m_i = 0$		$m_i = -1$	
		$P_{1/2}$ (mW) ^a	ε ^b	$P_{1/2}$ (mW) ^a	ε ^b	$P_{1/2}$ (mW) ^a	ε ^b
NONA ₉		11.5	1.02	14.4	1.02	18.5	1.18
NONA _{2,8}		23.2	1.09	26.9	1.11	31.5	1.18
	$\Delta P_{1/2}$	11.7	N.A.	12.5	N.A.	13	N.A.
OCTA ₇		11.3	0.95	13.3	0.94	16.9	1.1
OCTA _{2,7}		16.8	0.87	19.8	1.02	24.4	1.05
	$\Delta P_{1/2}$	5.6	N.A.	6.5	N.A.	7.5	N.A.
HEPTA ₆		13.1	0.83	16.8	0.84	21.2	1.02

		$M_i = +1$		N.A.	$M_i = -1$		
		$P_{1/2}$ (mW)	ε		$P_{1/2}$ (mW)	ε	
HEXA _{1,5}		58.6	1.5			58.6	1.5
	$\Delta P_{1/2}$ ^c	45.5	N.A.			37.4	N.A.
HEPTA _{3,6}		> 200	N.A.			> 200	N.A.
	$\Delta P_{1/2}$ ^c	> 200	N.A.		> 200	N.A.	

^a The error in $P_{1/2}$ due to fitting is less than 2%.

^b The error in ε due to fitting is less than 2%, except for HEXA_{1,5}: less than 5%.

^c with respect to $M_i = +1$ and $M_i = -1$ in HEPTA₆.

With values for $P_{1/2}$ and ε , we can in principle use equation 4.3 to calculate the product $T_1 T_2$ of the peptides. However, the resonator efficiency Λ of the dielectric cavity has to be determined first. Finding Λ is presently under study. For now, we shall analyse the data in terms of $\Delta P_{1/2}$, which is the difference between the $P_{1/2}$ values of the mono- and bi-radicals:

$$\Delta P_{1/2} = P_{1/2 \text{ biradical}} - P_{1/2 \text{ monoradical}} \quad (4.5)$$

The resulting $\Delta P_{1/2}$ values are listed in Table 4.1. Notably, for peptides NONA_{2,8}, and OCTA_{2,7} the $\Delta P_{1/2}$ values do not differ significantly with respect to m_i .

4.4 Discussion

Reliable power-saturation curves have been obtained for all species investigated in this study. By excluding oxygen from the samples, Heisenberg exchange by oxygen as an additional relaxation source is avoided.

Saturation behaviour is expressed in the parameters ε and $P_{1/2}$. We first discuss the ε parameters of all compounds. The ε values agree with the results of the lineshape simulations performed previously, with the exception of HEXA_{1,5}. The latter bi-radical saturates as a pure Lorentzian ($\varepsilon = 1.5$), whereas the lineshape was simulated with a mixture of Gaussian and Lorentzian lines. The origin of this discrepancy may be the two-component nature of the cw-EPR spectrum (see below). The fast relaxation in HEPTA_{3,6} prevents the determination of ε .

Equation 4.3 shows that $P_{1/2}$ is inversely proportional to the product T_1T_2 , therefore, large $P_{1/2}$ values are identified with fast relaxation and, unless specified otherwise, we refer to relaxation as the product of the two relaxation times.

The parameters obtained for $P_{1/2}$ show systematic trends. For the mono-radicals and the class II bi-radicals, the $P_{1/2}$ values decrease with increasing m_i , suggesting a spin-spin relaxation process, because, for nitroxides, the spin-spin relaxation time T_2 is m_i dependent^[10-13] which is not the case for T_1 , see for example^[14]. In particular, T_2 increases with increasing m_i , and since T_2 is inversely proportional to $P_{1/2}$, a decrease in $P_{1/2}$ with increasing m_i is fully consistent with a T_2 process.

To compare the mono- and bi-radical relaxation we use the difference of $P_{1/2}$ values ($\Delta P_{1/2}$, equation 4.5). To avoid interference from different

relaxation mechanisms, $\Delta P_{\frac{1}{2}}$ values are given for the same m_i – transitions as much as possible.

The two class I bi-radicals HEPTA_{3,6} and HEXA_{1,5} are in the regime of strong exchange interaction^[4] and, considering their $P_{\frac{1}{2}}$ values (Table 4.1), relax significantly faster than their mono-radical reference HEPTA₆ and the class II bi-radicals. For HEPTA_{3,6} this relaxation is even so fast that only a lower limit for $P_{\frac{1}{2}}$ can be given. The saturation of three of the five lines of the HEXA_{1,5} bi-radical (components $M_I = \pm 2$ and 0) could not be fitted to equation 4.2, whereas the $M_I = \pm 1$ components could. Previously, the EPR spectra of this bi-radical were shown to consist of two species, one that has a five-line spectrum and one with a three-line spectrum, the three lines of which overlap with the $M_I = \pm 2$ and 0 lines of the five-line spectrum. The two species were speculated to derive from two conformations of the bi-radical, a majority-fraction with a high J value and a minority-fraction of low J ^[4]. The presence of two species with presumably different relaxation behaviour that contribute to the $M_I = \pm 2$ and 0 components will produce power saturation curves that consist of a superposition of curves with different $P_{\frac{1}{2}}$ and ε values. We could not find models that consistently describe these curves, presumably due to the large number of parameters that have to be fit. The $\Delta P_{\frac{1}{2}}$ values given for HEXA_{1,5} derive from the $M_I = \pm 1$ components of the bi-radical and the $m_i = \pm 1$ of the mono-radical. The $M_I = \pm 1$ line connects $m_i = 0$ and $m_i = \pm 1$ transitions, and therefore, the $\Delta P_{\frac{1}{2}}$ value can contain a contribution, which is m_i dependent.

The $P_{\frac{1}{2}}$ values of class II bi-radicals, similar to the class I bi-radicals, are larger than their mono-radical references. The $\Delta P_{\frac{1}{2}}$ values hardly depend on

m_i , an indication that mono- and bi-radical have similar T_2 values. This is expected, because the spin-spin relaxation time T_2 is associated with the rotation-correlation time of the peptides, and mono- and bi-radical peptides are size-matched and therefore should have very similar rotation-correlation times. This also shows that the additional relaxation mechanism operating in the bi-radicals is most likely a T_1 -process. So we speculate that the spin-spin interaction in the bi-radicals opens another channel for T_1 relaxation.

In all four bi-radicals an additional relaxation process must be operative, and for the class II bi-radicals we show evidence that it is likely to be a T_1 process. For class I bi-radicals the additional relaxation process is stronger, leading to larger $\Delta P_{1/2}$ values than in class II bi-radicals. A quantitative comparison for class I bi-radicals is not straightforward. The $\Delta P_{1/2}$ values of one of these bi-radicals (HEXA_{1,5}) contains a contribution from different m_i transitions, and in that case we cannot exclude that also T_2 affects the $\Delta P_{1/2}$ values. For the second one of the class I bi-radicals, HEPTA_{3,6}, only a lower limit for $P_{1/2}$ and therefore $\Delta P_{1/2}$ could be given. Qualitatively, the bi-radical with the shortest distance between the nitroxides, HEPTA_{3,6}, has the fastest relaxation.

Within the class II bi-radicals, the $\Delta P_{1/2}$ value is larger for NONA_{2,8} than for OCTA_{2,7}, although for the latter peptide the TOAC residues are closer in the sequence. The through-space distance between the nitroxides in NONA_{2,8} (1.26 nm) is shorter than for OCTA_{2,7} (1.46 nm), showing that the mechanism causing the additional relaxation in class II bi-radicals is related to through-space interactions, rather than through-bond interactions.

Spin-spin interaction can enhance relaxation via the dipole-dipole interaction or via the exchange interaction J . The dipole-dipole interaction

depends only on the distance between the spins, whereas J , generally thought to depend exponentially on distance, also can have a substantial through-bond component. The difference in relaxation of NONA_{2,8} and OCTA_{2,7} cannot be due to a through-bond exchange mechanism, because that would cause faster relaxation in OCTA_{2,7} opposite to what we observe. Also a through-space J interaction mediated process is not likely, because the distances between the spins in both bi-radicals seem too long given the exponential decay of J with distance. Therefore, the dipolar interaction is the most likely candidate. To properly assess this point detailed quantum-mechanical calculations are needed, which we are starting off.

In summary, the important finding is that by power saturation we can discriminate between two bi-radicals, NONA_{2,8} and OCTA_{2,7}. These peptides have distances between the spin labels (1.26 nm and 1.46 nm, respectively) in a region that is difficult to address, and have almost identical cw-EPR spectra.

4.5 Conclusions

We show that meaningful power-saturation curves can be obtained at room temperature and at concentrations relevant for biological samples. The signal-to-noise ratio is sufficient to extract the relaxation parameters. We show that two bi-radical peptides, whose cw-EPR spectra are almost identical to those of their related mono-radicals, can be distinguished by their relaxation behaviour, showing that relaxation could be a monitor for distances of about 1.3 and 1.5 nm, right in the range that is difficult to assess for EPR distance determination.

References

- [1] A.D. Milov, A.G. Maryasov, Y.D. Tsvetkov, Pulsed electron double resonance (PELDOR) and its applications in free-radicals research. *Applied Magnetic Resonance* **15** (1998) 107-143.
- [2] G. Jeschke, Distance measurements in the nanometer range by pulse EPR. *Chemphyschem* **3** (2002) 927-932.
- [3] J.E. Banham, C.M. Baker, S. Ceola, I.J. Day, G.H. Grant, E.J.J. Groenen, C.T. Rodgers, G. Jeschke, C.R. Timmel, Distance measurements in the borderline region of applicability of CW EPR and DEER: A model study on a homologous series of spin-labelled peptides. *Journal of Magnetic Resonance* **191** (2008) 202-218.
- [4] M.H. Shabestari, M. van Son, A. Moretto, M. Crisma, C. Toniolo, M. Huber, Conformation and EPR Characterization of Rigid, 3(10)-Helical Peptides with TOAC Spin Labels: Models for Short Distances. *Biopolymers* **102** (2014) 244-251.
- [5] S. Carlotto, M. Zerbetto, M.H. Shabestari, A. Moretto, F. Formaggio, M. Crisma, C. Toniolo, M. Huber, A. Polimeno, In Silico Interpretation of cw-ESR at 9 and 95 GHz of Mono- and bis- TOAC-Labeled Aib-Homopeptides in Fluid and Frozen Acetonitrile. *Journal of Physical Chemistry B* **115** (2011) 13026-13036.
- [6] M. Zerbetto, S. Carlotto, A. Polimeno, C. Corvaja, L. Franco, C. Toniolo, F. Formaggio, V. Barone, P. Cimino, Ab initio modeling of CW-ESR spectra of the double spin labeled peptide Fmoc-(Aib-Aib-TOAC)(2)-Aib-OME in acetonitrile. *Journal of Physical Chemistry B* **111** (2007) 2668-2674.
- [7] C.P. Poole, *Electron Spin Resonance*, Wiley, New York, 1983.
- [8] C. Altenbach, W. Froncisz, R. Hemker, H. Mchaourab, W.L. Hubbell, Accessibility of nitroxide side chains: Absolute Heisenberg exchange rates from power saturation EPR. *Biophysical Journal* **89** (2005) 2103-2112.
- [9] W. Froncisz, J.S. Hyde, The Loop-Gap Resonator - A New Microwave Lumped Circuit Electron-Spin-Resonance Sample Structure. *Journal of Magnetic Resonance* **47** (1982) 515-521.
- [10] P.W. Atkins, D. Kivelson, ESR Linewidths in Solution .2. Analysis of Spin-Rotational Relaxation Data. *Journal of Chemical Physics* **44** (1966) 169-174.
- [11] D.E. Budil, S. Lee, S. Saxena, J.H. Freed, Nonlinear-least-squares analysis of slow-motion EPR spectra in one and two dimensions using a modified Levenberg-Marquardt algorithm. *Journal of Magnetic Resonance Series A* **120** (1996) 155-189.
- [12] R. Cassol, A. Ferrarini, P.L. Nordio, Dynamics of Nitroxide Probes Linked to Flexible Chains. *Journal of Physical Chemistry* **97** (1993) 2933-2940.
- [13] G. Moro, P.L. Nordio, U. Segre, Electron-Spin-Resonance Lineshapes of Free-Radicals Undergoing Jump Diffusion. *Gazzetta Chimica Italiana* **109** (1979) 585-588.
- [14] C. Galli, J.B. Innes, D.J. Hirsh, G.W. Brudvig, Effects of dipole-dipole interactions on microwave progressive power saturation of radicals in proteins. *Journal of Magnetic Resonance Series B* **110** (1996) 284-287.

5

EQUILIBRIUM UNFOLDING OF FLAVODOXIN FROM DOUBLE ELECTRON-ELECTRON RESONANCE DISTANCE CONSTRAINTS

5.1 Introduction

Protein folding is one of the most fascinating aspects of protein biochemistry. Insight into the process requires structural information on the protein chain at different folding states. Novel methods are sought to obtain experimental data on the folding process. Electron-paramagnetic-resonance techniques are well suited to follow the folding process, because they can determine distances and dynamics. Several EPR studies targeting folding of proteins have been reported, either based on steady-state^[1;2] or flow methods^[3-7].

Here we describe double electron-electron spin resonance (DEER) experiments performed under equilibrium unfolding conditions. The goal is to directly monitor *local* structure of the protein during unfolding by monitoring the distance between spin labels. Previous studies employing EPR were focused on local mobility changes, for example^[1;3], or distance measurements by EPR-line broadening^[4].

The present study describes the unfolding of holo-flavodoxin with guanidine hydrochloride (GuHCl)^[8] as unfolding agent. Flavodoxin folding has been the subject of several studies^[8-14]. The native-state structure of holo-flavodoxin is shown in Figure 5.1. Site-directed, spin-label mutagenesis was

performed to replace the native residue at position 131 by a cysteine. The native cysteine at position 69 serves as the second site for spin labelling with the nitroxide spin label MTSL. In the following we refer to the spin-labelled protein as fdx-SL. By DEER, we measure the distance between the two spin-label nitroxide groups. We interpret the distance in the native state, i.e., in the absence of GuHCl and the development of the distance distribution as a function of GuHCl concentration.

We demonstrate that we can follow the unfolding by DEER and detect changes in local structure upon unfolding. The distance distributions reveal the presence of proteins in conformations that are different from the native state and have well defined structure, indicative of folding intermediates.

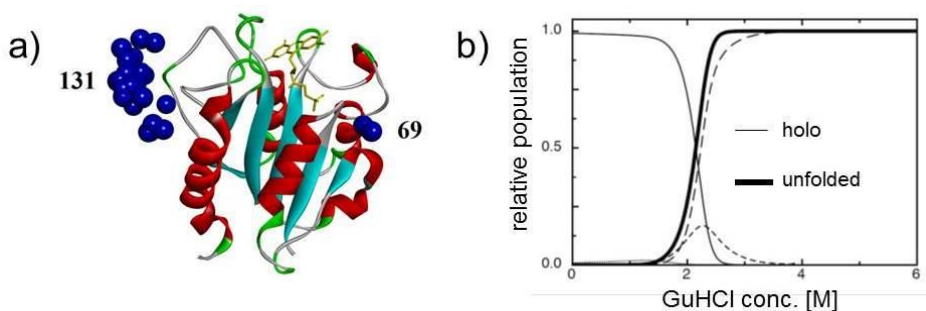


Figure 5.1 The structure of flavodoxin (fdx) based on the crystal structure (PDB entry 1YOB) with the flavine cofactor (in yellow). The blue spheres show representative locations of the nitroxide of the spin label, which is attached at positions 69 and 131 in the protein, as derived from the MMM simulation of protein A in the crystallographic unit cell. b) Normalized equilibrium population of holo-fdx (thin solid line), native apo-fdx (dots), off-pathway molten globule (short dashes) and unfolded protein (long dashes) as determined in reference [9]. The thick solid line represents the fraction of non-native molecules (i.e., the sum of off-pathway intermediate and unfolded protein).

5.2 Material and methods

Purification and spin labelling of flavodoxin D131C

The apo-fdx mutant D131C was generated and purified as described elsewhere^[8]. This variant contains the wild-type cysteine residue at position 69 as well as a cysteine residue at position 131. Prior to labelling of the protein with spin-label MTSL (Toronto Research Chemicals), the protein was unfolded in 5 M GuHCl, and incubated with dithiothreitol DTT to reduce the thiol-groups of the cysteines. The reductant DTT was removed by gel filtration with a P6-DG column (Bio-Rad), which was equilibrated with 5 M GuHCl (Fluka) in 50mM potassium phosphate (Sigma-Aldrich) buffer at pH 7.5. Labelling with MTSL was carried out during 16 hours at 4 °C, using a 20-fold molar excess of spin label over protein. The resulting doubly spin-labelled protein was purified from excess spin label and GuHCl by gel filtration on a Superdex 75 10/30 HR column (Pharmacia), which was equilibrated in 100 mM potassium pyrophosphate (Sigma-Aldrich) at pH 6.0. The apo-fdx thus obtained was incubated with an excess of flavin mononucleotide (FMN) to reconstitute the holoprotein. Free FMN was separated from holo-fdx by gel filtration on a Superdex 75 10/30 HR column.

The purification and spin labelling of flavodoxin was done by Simon Lindhoud (Laboratory of Biochemistry at Wageningen University and Research Centre).

Sample preparation

Guanidine hydrochloride (GuHCl) was used as a denaturant for the folding study. Due to the hygroscopy of GuHCl, it was not possible to use conventional means to prepare solutions with this compound in accurate concentrations.

Instead, we made a stock solution with an accurate concentration of GuHCl by measuring the refractive index of this solution and by using the relation

$$Z = 57.147\Delta N + 38.68(\Delta N)^2 - 91.60(\Delta N)^3, \quad (5.1)$$

where Z is the concentration of GuHCl in M and ΔN is the difference between the refractive indices of the buffer solution with and without GuHCl^[15]. The final concentrations of GuHCl used in the DEER measurements are mentioned in Table 5.1.

In each of the measurements, the protein concentration was about 0.1 mM. The buffer was 100 mM potassium pyrophosphate (KPP_i), pH 6.0, with 20% glycerol. The protein solutions were placed in quartz tubes with an id/od of 2.3 mm/3.0 mm. The samples that contained GuHCl were incubated at room temperature and in the dark for 12 hours.

A quantitative analysis of the spin-label concentration was made by double integration of the 80 K cw-EPR spectrum and comparison to the spectrum of MTSL with known spin concentration. Based on this analysis, we found that at least 83% of the fdx cysteines were spin labelled. The cw-EPR spectrum of a doubly labelled species is expected to show line broadening compared to the spectrum of a monoradical reference, when measured under the same conditions, if the spin labels are separated by less than 2 nm^[16].

Continuous wave EPR-measurements

The cw-EPR measurements were performed at 9.8 GHz using an ELEXSYS E 680 spectrometer (Bruker BioSpin GmbH, Rheinstetten, Germany) equipped with a rectangular cavity and a cryostat. A flow of liquid helium was directed through the cavity to maintain a temperature of 80 K. The spectra were recorded at a microwave power of 0.16 mW with a field sweep of 20 mT and

2048 field points. Field modulation at a frequency of 100 kHz was employed with an amplitude of 0.2 mT. The time constant was 41 ms with a conversion time of 41 ms. The measurement time was 15 to 30 minutes per sample.

DEER measurements and data analysis

The four-pulse DEER experiments were performed at 9.3 GHz using an ELEXSYS E 680 spectrometer (Bruker BioSpin GmbH, Rheinstetten, Germany) equipped with a split-ring cavity and a cryostat, Oxford model CF 935. A flow of liquid helium was directed through the cavity to maintain a temperature of 40 K. The DEER sequence is described in section 1.4. The separation between the frequencies was about 65 MHz. The observer pulses had lengths of 16 and 32 ns, the pump pulse had a length of 16 ns. The delay times were $\tau_1 = 140$ ns and $\tau_2 = 3.6$ μ s. The total time of a DEER measurement was about 15 hours.

Each of the DEER measurements was directly followed by a reference measurement. The sample for these reference measurements was a solution of a rigid biphenyl bi-radical in methyl tetrahydrofuran, contained in a quartz tube with an id/od of 2.3 mm/3.0 mm. Oxygen had been removed from the solution by four repeated freeze-thaw cycles, followed by flame sealing to close the tube.

The DEER data was analysed and fit with the DeerAnalysis2011 program^[17]. We assumed a homogenous three-dimensional background. The validation option within the software was used to find a consistent background start, resulting in 600 ns for the protein solutions with low denaturant concentrations (0, 0.3 M, 0.8 M, and 2.3 M) and 1720 ns for the high concentrations (3.5 M and 4.5 M).

5.3 Results

We study the unfolding of the doubly spin-labelled fdx mutant 131C (fdx-SL), which contains a native cysteine at position 69 and an engineered cysteine at position 131. The protein used is 85% spin labelled (see Materials and methods) and the sample did not contain free spin label, as determined by cw EPR experiments at room temperature (data not shown).

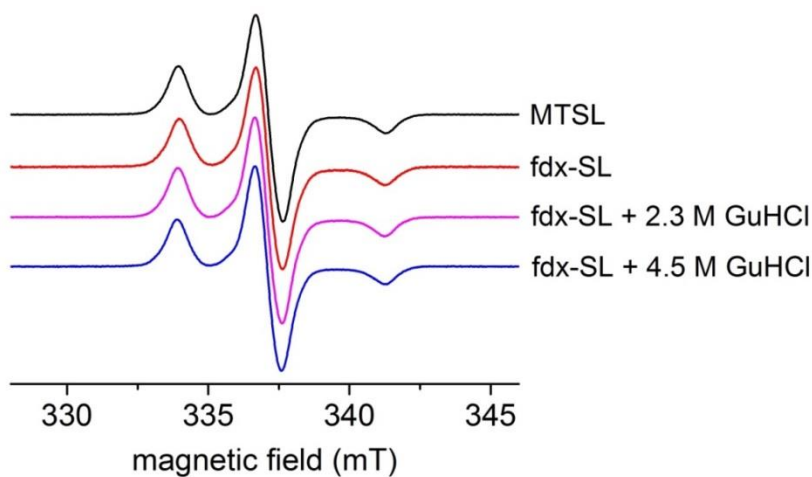


Figure 5.2 The cw-EPR spectra recorded at 80 K of MTSL (black), native fdx-SL (red), fdx-SL + 2.3 M GuHCl (pink), and fdx-SL + 4.5 M GuHCl (blue). The spectra are shifted vertically for better viewing.

The results of frozen solution cw EPR are shown in Figure 5.2. Regarding the lineshape, the cw-EPR spectra of the protein in frozen solution are identical to the spectra of a monomeric reference, thus no line broadening was detected. In Figure 5.3, all DEER-time traces are collected. Figure 5.3a shows the raw time traces and the background, and Figure 5.3b the background corrected traces. First, we will describe the results obtained on fdx-SL in the native state, i.e., in

the absence of GuHCl, and then we will describe the results of the series of DEER experiments performed on fdx-SL at different GuHCl concentrations.

The DEER-time trace of fdx-SL in the absence of GuHCl, shown in Figure 5.3a, has an initial decay and hardly any structure, i.e., visible modulation. The modulation depth corresponds to that expected for two coupled spins, which shows that the entire protein population contributes to the distance distribution shown in Figure 5.4. The distribution has two peaks with maxima at 3.77 nm and 4.62 nm, i.e., separated by 0.85 nm and widths (full width at half maximum - fwhm) of 0.37 nm and 0.39 nm, respectively. The peak at 3.77 nm has a shoulder at shorter distances indicating a third distance component.

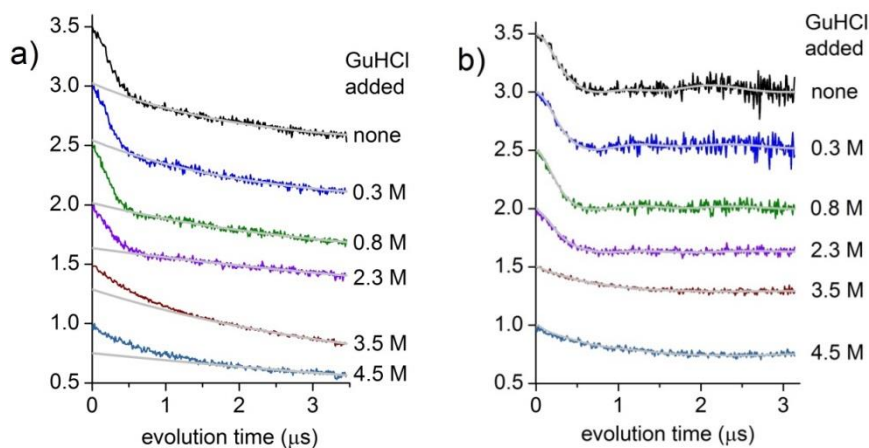


Figure 5.3 The DEER traces for fdx-SL measured at different concentrations of GuHCl. a) The traces obtained from the DEER measurements are shown with their optimal background fit (in grey). Individual traces are normalized and shifted vertically for better viewing. b) The traces obtained after division by the background fit. In b) the fitted traces (in grey) correspond to distance distributions ($\alpha = 100$) that are shown in Figure 5.4 and 5.5b.

The measured distances are between the nitroxide groups of the two spin labels. Each nitroxide group is separated from the protein backbone by the spin-label linker, which has a length of about 0.5 nm. Therefore, the spin-label linker has to be taken into account to relate the distance measured by DEER to the protein structure. Spin-label-linker conformations were calculated by the rotamer-library based method MMM^[18] with the X-ray structure of holo-fdx as input (PDB entry 1YOB^[19]). The X-ray structure of fdx contains two proteins in the asymmetric unit of the crystal (monomer A and monomer B). The distance distributions calculated for the two proteins in the asymmetric unit are shown in Figure 5.4. The MMM distance distributions of both monomers, A and B, each have two peaks, which are separated by 0.38 nm (monomer A) and 0.40 nm (monomer B). The two peaks derive from two families of linker conformations, since, in the X-ray structure, the protein backbone has a unique conformation. In Figure 5.1 selected locations of the nitroxide are shown as spheres. Particularly, the spin label at position 69 has only few accessible conformations, whereas the spin label at 131 has an extensive cloud of nitroxide positions, suggesting that the two families derive from two sets of conformations of the spin label at position 69. The centres of the distributions of monomer A and B differ by 0.15 nm. Figure 5.4 further shows that the distributions derived from the X-ray structure are centred at shorter distances than those obtained from the DEER measurement at 0.3 M GuHCl. The distance distribution at 0.3 M GuHCl (Figure 5.5), differs from that of fdx-SL in the absence of GuHCl (Figure 5.4), although for both samples the protein should still be fully folded^[8].

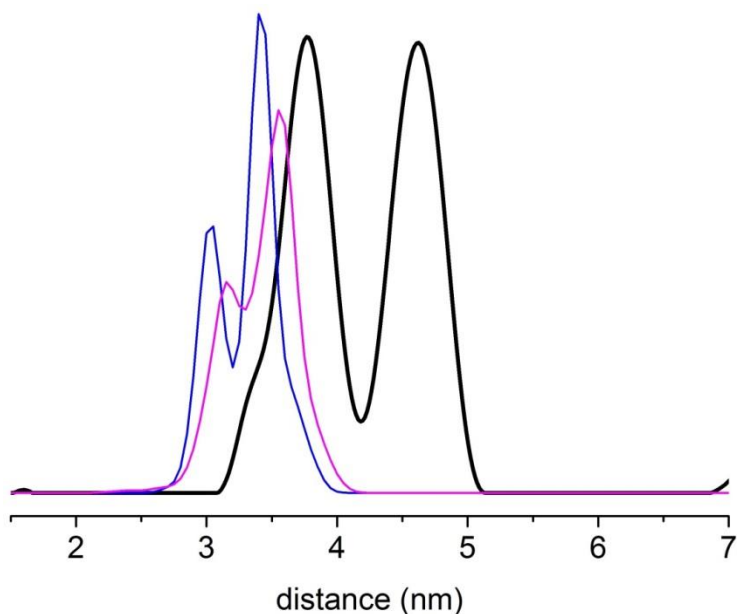


Figure 5.4 Distance distribution of native fdx-SL with regularization parameter 100 (black) and those derived by simulation with MMM from the crystal structure of fdx (blue, purple). Crystal structure: PDB entry 1YOB, using monomers A and B in the crystallographic unit cell.

Figure 5.5a and b show distance distributions obtained at different GuHCl concentrations. Data from two regularization parameters^[20] are shown: a) appropriate for the distributions at GuHCl concentrations ≤ 2.3 M and b) for > 2.3 M. To monitor the unfolding we use the distance distribution of 0.3 M GuHCl as a reference. With respect to the modulation depth (Figure 5.3b), the DEER data fall into two regimes: from 0.3 M to 2.3 M GuHCl, the modulation depth accounts for $> 94\%$ of the protein population. From 2.3 to 3.5 M GuHCl the protein population that contributes to the distance distribution halves (Table 5.1), showing that at 3.5 M GuHCl a large fraction of the protein is in conformations where the spin-spin distance of the two nitroxides is outside the measurement range of the DEER experiment, i.e., smaller than 2 nm and/or

larger than 6 nm. Given the low modulation depth, and the smooth decay of the DEER time trace, the exact shape of the distance distribution is less certain than the distribution for the lower GuHCl concentrations. A higher regularization parameter, i.e., $\alpha = 100$ has to be used to describe the distributions at 3.5 and 4.5 M properly, as will be discussed below.

Table 5.1 Overall parameters of the DEER derived distance distributions upon fdx unfolding. Parameters are derived from the distributions with regularization parameter 100.

concentration GuHCl (M)	coupled spins (%) ^a	mean distance $\langle r \rangle$ (nm)	standard deviation σ (nm)
0.3	109	4.08	0.45
0.8	117	4.01	0.51
2.3	94	4.25	0.58
3.5	40	5.3	1.55
4.5	48	5.38	1.62

^a Calculated from the number of spins: 2 = 100%, 1 = 0%. The number of spins yielded by DeerAnalysis has an overall error of about 5%, corresponding to an error of 10% in the percentage of coupled spins (see reference [21]).

To describe the distance distributions in Figure 5.5a, Gaussian bands are fitted to the most intense peaks (Figure 5.5c). Several smaller, less intense peaks, marked by an asterisk, were shown not to be significant by the suppression tool in DEER analysis, meaning that their contribution to the DEER time-trace does not cause a significant deviation, given the noise of the curve. The distributions at 0.3 M and 0.8 M GuHCl are well described by three Gaussians (labelled $N_1 - N_3$ in Table 5.2) with slightly different parameters for these two GuHCl concentrations. As an illustration, from 0.3 to 0.8 M GuHCl, the peak N_1 shifts by 0.16 nm to lower distances and all widths increase; the largest increase in

width is observed for the peak N_3 , which increases by 0.09 nm. The distribution at 2.3 M GuHCl requires five Gaussians. Three of them ($N_1 - N_3$) are similar to those observed at lower GuHCl concentrations. A new peak appears at 3 nm (MG_1) and a shoulder at peak N_2 shows an underlying additional peak (MG_2). The area under the MG_1 and MG_2 peaks accounts for in total 17% of the five Gaussians in the distribution.

Table 5.2 Parameters of the Gaussian fits of DEER distance distributions. X_c : centre of Gaussian, W: full width at half maximum, A: area under the curve at 0.3 M, 0.8 M, and 2.3 M GuHCl, regularization parameter 10.

peaks		GuHCl concentration			
		0	0.3 M	0.8 M	2.3 M
N_1	X_c (nm)	3.32	3.58	3.42	3.48
	W (nm)	0.13	0.22	0.23	0.16
	A	7%	22%	20%	9%
N_2	X_c (nm)	3.78	3.98	3.91	3.95
	W (nm)	0.28	0.27	0.35	0.38
	A	43%	49%	58%	49%
N_3	X_c (nm)	4.62	4.69	4.68	4.85
	W (nm)	0.36	0.27	0.36	0.55
	A	50%	29%	22%	25%
MG_1	X_c (nm)	N.A.	N.A.	N.A.	3.05
	W (nm)				0.15
	A				9%
MG_2	X_c (nm)	N.A.	N.A.	N.A.	4.29
	W (nm)				0.23
	A				8%

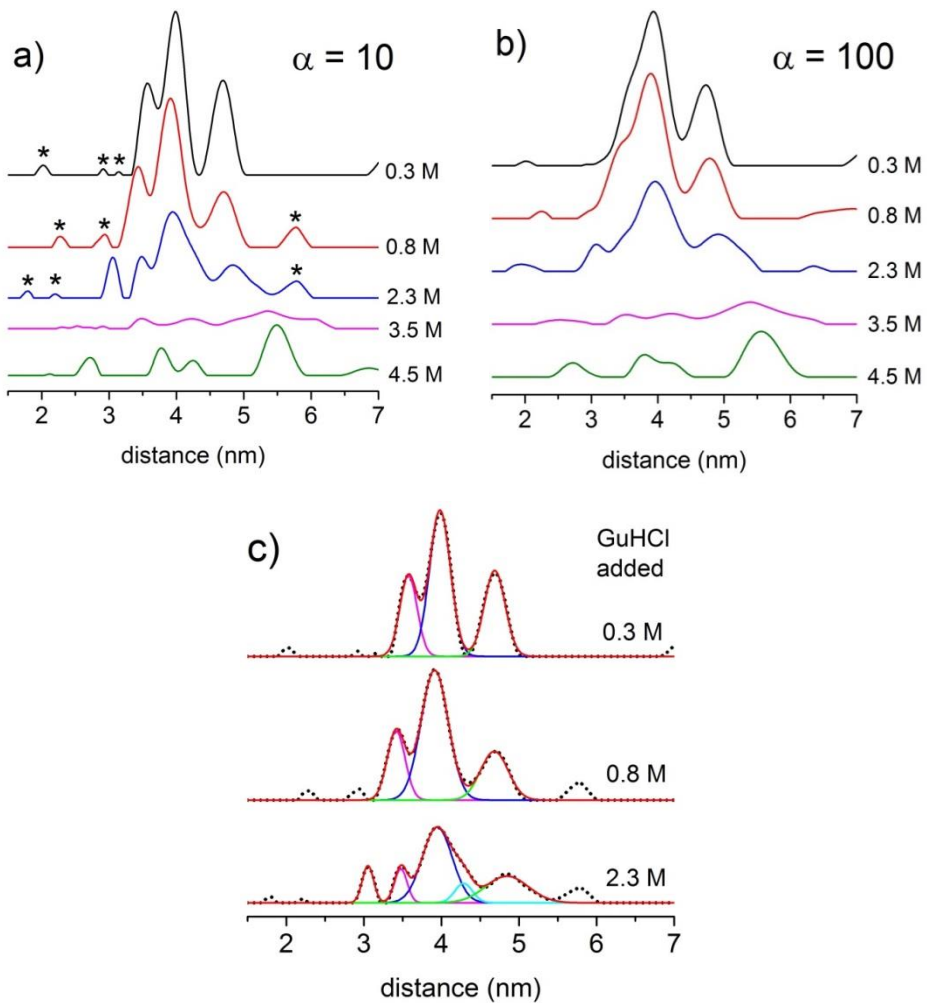


Figure 5.5 Effect of GuHCl concentration on distance distributions of fdx-SL. The distance distributions were obtained with the regularization parameter of a) $\alpha = 10$ and b) $\alpha = 100$, and c) fits of Gaussians to the top three distance distributions in a).

The mean distance of the distribution $\langle r \rangle$ and the width, given as the standard deviation σ , reveal the overall features of the distance distributions for all GuHCl concentrations (Table 5.1). The mean distance remains almost constant between 0.3 and 2.3 M GuHCl and increases by 1 nm at 3.5 and 4.5 M GuHCl, with concomitant tripling of the standard deviation. Figure 5.6 is a graphical representation of the data in Table 5.1.

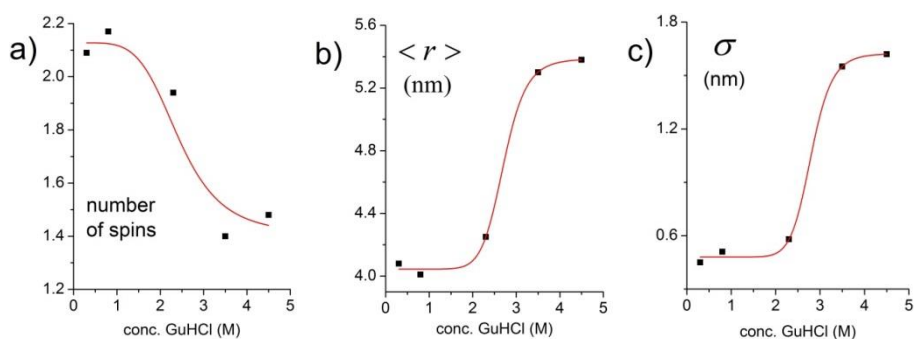


Figure 5.6 Representations of the unfolding of fdx-SL as a function of the concentration of GuHCl through three observables derived from the EPR experiments: a) the number of spins, b) the mean distance $\langle r \rangle$ for $\alpha = 100$, and c) the standard deviation σ for $\alpha = 100$. The red lines merely serve as a guide to the eye. The figures are graphical representations of the data in Table 5.1.

5.4 Discussion

We have investigated the unfolding of fdx in the presence of different amounts of the unfolding agent GuHCl. Before describing the changes in protein structure under the influence of the unfolding agent, the distance distribution of the native fdx is discussed in terms of what is known about the structure of fdx in the folded state.

The native state of holo-fdx

In the folded, native state, fdx is a globular protein with a well-defined, single structure. Nevertheless, there are two peaks in the distance distribution of the native protein (Figure 5.4), the widths of which are typical of the intrinsic flexibility of the spin-label side chain attached to a well-structured protein^[22]. Modelling the spin-label side-chain conformation with MMM also yields two-peaked distance distributions, albeit at shorter distances than observed experimentally, showing that the two distances observed in the measured distance distribution stem from two families of spin-label linker conformations. The overall longer distances measured could derive from a more extended conformation of the loop between residues 126 to 148, which contains one of the spin-label sites, residue 131. Changes in the conformation of the loop will affect the mutual distance between the spin labels at position 131 and 69. The second factor is the protein structure around the cysteine at position 69. In the native protein, the cysteine at this position points to the interior of the protein. In the spin-labelled state, this cysteine is more likely to switch to a conformation that projects the spin-label side chain to the exterior of the protein, thereby increasing the distance between the nitroxides of the two spin labels. Such a change in the side-chain and backbone conformation is not accounted for in MMM, explaining the difference between the MMM and the DEER-derived distances of the native protein. The distance distribution

observed by DEER, therefore, is compatible with what is known about the native structure of fdx. At a GuHCl concentration of 0.3 M, the protein is in the fully folded state^[8], however, the distance and distance distribution differs slightly from that of fdx in the absence of GuHCl: The peak at 3.8 nm splits into two, leading to a three-peaked distance distribution described by the Gaussian peaks $N_1 - N_3$. We attribute these changes to a local influence of GuHCl on the spin-label conformation.

Unfolding of fdx followed by DEER

Similarly to previous EPR studies on other proteins^[1;3], also for fdx we find systematic changes of the EPR parameters with respect to the GuHCl concentration, showing that DEER provides a method to follow protein unfolding. To analyse the changes in detail, we use the distance distribution of 0.3 M GuHCl as a reference to ensure that the effects of GuHCl derive from the unfolding of the protein and not from a local influence of GuHCl on the spin-label conformation.

According to the DEER results, the most remarkable change in the structure of fdx during unfolding occurs between 2.3 and 3.5 M GuHCl. Up to a concentration of 2.3 M GuHCl, the distance distributions account for almost the entire protein population and the shape of the distance distribution is that of a structured protein. At 3.5 and 4.5 M GuHCl, the distance distributions become broader and the average distance $\langle r \rangle$ becomes larger with increasing GuHCl concentrations (Table 5.1). A larger fraction of fdx-SL has distances that are outside the DEER observation window, i.e., below 2 nm or above 6.5 nm. Distances below 2 nm can be excluded, because they would give rise to a dipolar broadening in the frozen solution cw EPR spectra, which does not occur (see Results). In summary, the protein goes from a state with a limited number of conformations and a relative compact structure at lower GuHCl

concentrations to a large number of conformations and a more extended state at GuHCl concentrations of 3.5 M and above, in keeping with a largely unfolded state. In the following we take a closer look at the lower GuHCl concentrations.

At concentrations of 2.3 M GuHCl and below, the protein has all characteristics of a structured protein. To interpret the results at these lower GuHCl concentrations, we take the three-peak distance distribution ($N_1 - N_3$, Table 5.2) in Figure 5.5a, 0.3 M GuHCl, as the signature of natively folded protein. Thus, at 0.8 M GuHCl, the protein is predominantly in the native conformation. There are small differences between the parameters of $N_1 - N_3$ at 0.3 and 0.8 M GuHCl, which we interpret as changes in the local spin-label environment by GuHCl (Table 5.2).

At 2.3 M GuHCl, additional distance peaks (MG_1 and MG_2 , Figure 5.5a and c, Table 5.2) appear. The widths of these peaks are in the order of the widths of the native state peaks, showing that in the corresponding state the protein has a well-defined structure. To estimate the populations of the different states of the protein at 2.3 M GuHCl, not only the relative contribution of the distance peaks MG_1 and MG_2 to the remaining peaks $N_1 - N_3$, but also the 15% of protein with distances outside the DEER range are taken into account. Total populations of 72% native, 14% folding intermediate, and 15% unfolded protein result. In this interpretation we count the entire population under the peaks $N_1 - N_3$ as native protein, however, this need not be. The relative intensities of the peaks N_1 , N_2 and N_3 at 2.3 M GuHCl are not identical to those at lower GuHCl concentrations. The deviation is largest for N_1 , which has an intensity that is 11% smaller than in the native protein (0.3 M GuHCl). A folding intermediate that accidentally has a distance similar to one of the native ones, or, perhaps more likely, an underlying broader distance distribution, could change the apparent relative intensities of the peaks $N_1 - N_3$. We, therefore, consider the native state population of 72% as an upper limit.

Counting, somewhat arbitrarily, the entire loss of intensity at N_1 as population of folding intermediate would result in 61% native and 25% folding intermediate, which we estimate to be lower limits of native-state population, and upper limits of folding-intermediate population, respectively.

Therefore, we postulate that between 14% and 25% of the protein at 2.3 M GuHCl are in a folding-intermediate state, characterized by distance contributions MG_1 and MG_2 . Given that the MG_1 and MG_2 distances differ by 1.24 nm, MG_1 and MG_2 presumably reflect proteins in different conformations, rather than a single backbone conformation with different families of nitroxide side-chain orientations. Consequently, a certain population of the protein attains a fold, in which residues 69 and 131 are closer to each other than in the native state (MG_1), and one in which the distance is intermediate amongst the distances seen in the native state (MG_2).

The presence of a folding intermediate was also suggested by recent single-molecule Förster resonance energy-transfer (FRET) experiments, which targeted the distance between the same two positions^[23]. Below about 1.5 M GuHCl, this intermediate has a shorter inter-dye distance than the native protein. At higher GuHCl concentrations, this intermediate gradually unfolds into a less well-structured state, characterized by longer distances than in the native protein. The coexistence of the intermediate with the native-like protein seemed to occur at overall lower GuHCl concentrations than in the present EPR study. This is reasonable, given that in the optical study apo-fdx was investigated, which has a lower stability and therefore unfolds at lower GuHCl concentrations than the holo-fdx we study here. Furthermore, differences are to be expected because the labels are different. For EPR nitroxide spin labels are used, whereas the labels used in the FRET-experiments are more bulky and could additionally destabilize the folding intermediate. Further differences

could arise from the different intervals between the GuHCl concentrations in both studies.

We show that by DEER local structure in the unfolding protein can be measured and present evidence for a folding intermediate that is locally more compact than the native state and is in coexistence with a folding intermediate that has a distance between residues 69 and 131 that is similar to the native state. The DEER method provides distance distributions. Their widths give information about the degree of structure of a particular state and thereby enable us to discriminate between unfolded states and folding intermediates.

References

- [1] D.I. Kreimer, R. Szosenfogel, D. Goldfarb, I. Silman, L. Weiner, 2-State Transition Between Molten Globule and Unfolded States of Acetylcholinesterase As Monitored by Electron-Paramagnetic-Resonance Spectroscopy. *Proceedings of the National Academy of Sciences of the United States of America* **91** (1994) 12145-12149.
- [2] W.L. Hubbell, H.S. Mchaourab, C. Altenbach, M.A. Lietzow, Watching proteins move using site-directed spin labeling. *Structure* **4** (1996) 779-783.
- [3] K. Deweerd, V. Grigoryants, Y.H. Sun, J.S. Fetrow, C.P. Scholes, EPR-detected folding kinetics of externally located cysteine-directed spin-labeled mutants of iso-1-cytochrome c. *Biochemistry* **40** (2001) 15846-15855.
- [4] V.M. Grigoryants, K.A. DeWeerd, C.P. Scholes, Method of rapid mix EPR applied to the folding of bi-spin-labeled protein as a probe for the dynamic onset of interaction between sequentially distant side chains. *Journal of Physical Chemistry B* **108** (2004) 9463-9468.
- [5] V.M. Grigoryants, A.V. Veselov, C.P. Scholes, Variable velocity liquid flow EPR applied to submillisecond protein folding. *Biophysical Journal* **78** (2000) 2702-2708.
- [6] K.B. Qu, J.L. Vaughn, A. Sienkiewicz, C.P. Scholes, J.S. Fetrow, Kinetics and motional dynamics of spin-labeled yeast iso-1-cytochrome c .1. Stopped-flow electron paramagnetic resonance as a probe for protein folding/unfolding of the C-terminal helix spin-labeled at cysteine 102. *Biochemistry* **36** (1997) 2884-2897.
- [7] A. Sienkiewicz, A.M.D. Ferreira, B. Danner, C.P. Scholes, Dielectric resonator-based flow and stopped-flow EPR with rapid field scanning: A methodology for increasing kinetic information. *Journal of Magnetic Resonance* **136** (1999) 137-142.
- [8] S. Lindhoud, A.H. Westphal, J.W. Borst, C.P.M. van Mierlo, Illuminating the Off-Pathway Nature of the Molten Globule Folding Intermediate of an alpha-beta Parallel Protein. *Plos One* **7** (2012) 1-10.
- [9] Y.J.M. Bollen, S.M. Nabuurs, W.J.H. van Berkel, C.P.M. van Mierlo, Last in, first out. *Journal of Biological Chemistry* **280** (2005) 7836-7844.
- [10] S.M. Nabuurs, B.J. de Kort, A.H. Westphal, C.P.M. van Mierlo, Non-native hydrophobic interactions detected in unfolded apoflavodoxin by paramagnetic relaxation enhancement. *European Biophysics Journal with Biophysics Letters* **39** (2010) 689-698.
- [11] S.M. Nabuurs, C.P.M. van Mierlo, Interrupted Hydrogen/Deuterium Exchange Reveals the Stable Core of the Remarkably Helical Molten Globule of alpha-beta Parallel Protein Flavodoxin. *Journal of Biological Chemistry* **285** (2010) 4165-4172.
- [12] S.M. Nabuurs, A.H. Westphal, M. aan den Toorn, S. Lindhoud, C.P.M. van Mierlo, Topological Switching between an alpha-beta Parallel Protein and a Remarkably Helical Molten Globule. *Journal of the American Chemical Society* **131** (2009) 8290-8295.
- [13] S.M. Nabuurs, A.H. Westphal, C.P.M. van Mierlo, Noncooperative Formation of the Off-Pathway Molten Globule during Folding of the alpha-beta Parallel Protein Apoflavodoxin. *Journal of the American Chemical Society* **131** (2009) 2739-2746.

- [14] S.M. Nabuurs, A.H. Westphal, C.P.M. van Mierlo, Extensive Formation of Off-Pathway Species during Folding of an alpha-beta Parallel Protein Is Due to Docking of (Non)native Structure Elements in Unfolded Molecules. *Journal of the American Chemical Society* **130** (2008) 16914-16920.
- [15] B.A. Shirley, Urea and Guanidine Hydrochloride Denaturation Curves. *Protein Stability and Folding: Theory and Practice*, Humana Press, New Jersey, 1995, pp. 177-190.
- [16] G. Jeschke, Determination of the nanostructure of polymer materials by electron paramagnetic resonance spectroscopy. *Macromolecular Rapid Communications* **23** (2002) 227-246.
- [17] G. Jeschke, V. Chechik, P. Ionita, A. Godt, H. Zimmermann, J. Banham, C.R. Timmel, D. Hilger, H. Jung, DeerAnalysis2006 - a comprehensive software package for analyzing pulsed ELDOR data. *Applied Magnetic Resonance* **30** (2006) 473-498.
- [18] Y. Polyhach, E. Bordignon, G. Jeschke, Rotamer libraries of spin labelled cysteines for protein studies. *Physical Chemistry Chemical Physics* **13** (2011) 2356-2366.
- [19] S. Alagaratnam, G. Van Pouderoyen, T. Pijning, B.W. Dijkstra, D. Cavazzini, G.L. Rossi, W.M.A.M. Van Dongen, C.P.M. van Mierlo, W.J.H. van Berkel, G.W. Canters, A crystallographic study of Cys69Ala flavodoxin II from *Azotobacter vinelandii*: Structural determinants of redox potential. *Protein Science* **14** (2005) 2284-2295.
- [20] G. Jeschke, A. Koch, U. Jonas, A. Godt, Direct conversion of EPR dipolar time evolution data to distance distributions. *Journal of Magnetic Resonance* **155** (2002) 72-82.
- [21] B.E. Bode, D. Margraf, J. Plackmeyer, G. Durner, T.F. Prisner, O. Schiemann, Counting the monomers in nanometer-sized oligomers by pulsed electron - electron double resonance. *Journal of the American Chemical Society* **129** (2007) 6736-6745.
- [22] M.G. Finiguerra, M. Prudencio, M. Ubbink, M. Huber, Accurate long-range distance measurements in a doubly spin-labeled protein by a four-pulse, double electron-electron resonance method. *Magnetic Resonance in Chemistry* **46** (2008) 1096-1101.
- [23] S. Lindhoud *et al.*, data to be published.

SUMMARY

This thesis describes four studies of the structure and dynamics of biomolecules by electron paramagnetic resonance (EPR). In *Chapter 1*, the principles of this magnetic resonance are introduced.

Membrane fusion, the merging of one membrane vesicle with another, is an essential biomolecular process in eukaryotes. The mechanistic details of this fusion remain to be unravelled. Within this framework, *Chapter 2* presents a study on the interaction of two types of small biomolecules, the peptides E and K. The peptides are designed such that they form a heterodimer when mixed in solution, i.e., one type of peptide forms a dimer with the other type, but not with the same type of peptide. We have investigated the peptides by means of paramagnetic resonance and concluded that heterodimer formation is detectable by this technique. Next, we intend to couple the peptides to membrane vesicles. The model constructs created this way are expected to be capable of membrane fusion. Our ultimate goal is to apply EPR on the model constructs in order to reveal structural information of the constructs during membrane fusion.

Numerous types of protein-protein interactions are involved in cell metabolism, muscle contraction, and signal transduction. These interactions range from static to transient. *Chapter 3* reports on the investigation of the transient interaction between the proteins cytochrome *c* (Cc) and cytochrome *c* peroxidase (CcP). A spin label was placed at the surface of Cc. Conventional EPR (9 GHz) was applied to Cc mixed with different concentrations of CcP. The spectra show that the spin label becomes immobilized upon complex formation. Principal component analysis (PCA) was used to disentangle the EPR spectra. The analysis yielded two pure-component spectra, which

correspond to a slow fraction and a fast fraction of the spin label. The findings are in agreement with previous studies, which shows that the interaction of Cc and CcP involves a static, stereo-specific complex and a more dynamic, loosely bound encounter complex. The PCA analysis proved to be effective and – in combination with EPR – can be considered an excellent tool to study protein-protein interactions.

A useful way to obtain structural information of a biomolecule is by measuring the distance between two points, e.g. between two paramagnetic centres. Distances in the range of 1.5 nm to 6.0 nm are detectable by pulse EPR techniques. Distances shorter than 1.5 nm are more challenging to access. *Chapter 4* explores the possibility of relating the exchange interaction (J coupling) between two spins to short-range distances. We have investigated four peptides that each contain two spin labels, separated by two, three, four, or five amino acids. Previously, a continuous-wave EPR study had shown that in two of these peptides the J coupling is significantly larger than in the other two peptides. In the present study, power-saturation experiments were applied to the peptides to obtain spin-relaxation parameters. We observed that the rate of relaxation increases strongly when the spin labels are closer together. We attribute this to a correspondingly higher J coupling. This makes it possible to discriminate between pairs of spin labels at different positions in the peptides. We posit that power saturation experiments could be used as a tool for short-range distance determination. In contrast to pulse EPR to determine distances, power-saturation experiments can be done in liquid solution and at room temperature, both biologically relevant conditions.

Protein folding is a crucial process in every living cell. Correct protein folding generates a three-dimensional structure that is capable of carrying out a

biological function. Incorrect protein folding is thought to be the cause of certain diseases, such as cystic fibrosis and Alzheimer's disease. *Chapter 5* describes a novel method to obtain experimental data on the folding process. Two spin labels were placed at different positions in the protein flavodoxin. With double electron-electron spin resonance (DEER) we measured the distance between the spin labels on flavodoxin in different concentrations of denaturant. The distance distributions obtained by DEER show that local structure in the unfolding protein can be measured and present evidence for a folding intermediate that is locally more compact than the protein in its native state. We demonstrate that we can follow the unfolding of flavodoxin by DEER and detect changes in local structure upon unfolding.

SAMENVATTING

Dit proefschrift beschrijft vier onderzoeken aan de structuur en dynamica van biomoleculen met behulp van elektron paramagnetisch resonantie (EPR). In *Hoofdstuk 1* worden de principes van deze magnetische resonantietechniek geïntroduceerd.

Membraanfusie, het samengaan van twee membranen tot één, is in eukaryoten een essentieel biomoleculair proces. De details van het mechanisme van membraanfusie moeten nog worden ontrafeld. In dit kader beschrijft *Hoofdstuk 2* een studie van de interactie tussen twee typen van kleine biomoleculen, de peptiden E en K. De peptiden zijn zodanig ontworpen dat zij een heterodimeer vormen wanneer zij in oplossing gemengd worden, d.w.z. een type peptide vormt een dimeer met het andere type, maar niet met hetzelfde type peptide. We hebben de peptiden met EPR onderzocht en geconcludeerd dat de vorming van het heterodimeer gedetecteerd kan worden met deze techniek. In de volgende fase zijn wij van plan om de peptiden te koppelen aan membraanvesikels. Wij vermoeden dat de modelconstructen die zo ontstaan in staat zijn om membraanfusie te ondergaan. Ons uiteindelijke doel is om EPR toe te passen op de modelconstructen om informatie te verkrijgen over hun structuur tijdens membraanfusie.

Tallose vormen van eiwit-eiwit-interacties zijn betrokken bij celmetabolisme, spiercontractie en signaaloverdracht. Deze interacties variëren van statisch tot dynamisch. *Hoofdstuk 3* rapporteert over een studie naar de dynamische interactie tussen de eiwitten cytochroom *c* (Cc) and cytochroom *c* peroxidase (CcP). Een spinlabel werd op het oppervlak van Cc geplaatst. Conventionele EPR (9 GHz) werd toegepast op Cc in mengsels met verschillende

concentraties van CcP. De spectra laten zien dat het spinlabel geïmmobiliseerd wordt ten gevolge van complexvorming. *Principal component analysis* (PCA) werd gebruikt om de spectra te ontrafelen. De analyse leverde de spectra van twee zuivere componenten op die overeenkomen met een langzame fractie en een snelle fractie van het spinlabel. De bevindingen stemmen overeen met de resultaten van eerdere studies, wat aantoont dat zowel een statisch, stereospecifiek complex als een dynamischer, los gebonden *encounter complex* betrokken zijn bij de interactie tussen Cc en CcP. De PCA-analyse bleek effectief te zijn en kan – in combinatie met EPR – worden beschouwd als een uitstekend gereedschap om eiwit-eiwit-interacties te bestuderen.

Een nuttige manier om informatie te verkrijgen over de structuur van een biomolecuul is door de afstand tussen twee punten te meten, bijvoorbeeld tussen twee paramagnetische centra. Afstanden in het bereik van 1.5 nm tot 6.0 nm zijn goed waarneembaar met gepulste EPR-technieken. Afstanden kleiner dan 1.5 nm zijn moeilijker te meten. *Hoofdstuk 4* verkent de mogelijkheid om de *J*-koppeling (*exchange interaction*) tussen twee spins te relateren aan hun afstand. We hebben vier peptiden onderzocht, elk met twee spinlabels die gescheiden zijn door twee, drie, vier respectievelijk vijf aminozuren. Een voorafgaande *continuous-wave* EPR-studie heeft laten zien dat in twee van deze peptiden de *J*-koppeling significant groter is dan in de andere twee peptiden. In de huidige studie werden verzadigingsexperimenten toegepast op de peptiden om relaxatieparameters van de elektronspins te verkrijgen. We hebben gezien dat naarmate de spinlabels dichter bij elkaar zijn, de relaxatie sneller is, wat wij toeschrijven aan een navenant hogere *J*-koppeling. Dit maakt het mogelijk om onderscheid te maken tussen paren van spinlabels op verschillende posities in de peptiden. Wij concluderen dat verzadigingsexperimenten gebruikt kunnen worden voor het bepalen van korte

afstanden. In tegenstelling tot gepulste EPR-technieken om afstanden te bepalen, kunnen verzadigingsexperimenten worden uitgevoerd onder biologisch relevante condities, namelijk in oplossing en bij kamertemperatuur.

Eiwitvouwing is in iedere levende cel een cruciaal proces. Correcte vouwing van het eiwit leidt tot een driedimensionale structuur die in staat is om een biologische functie uit te voeren. Foutieve vouwing van het eiwit wordt als de oorzaak gezien van aandoeningen als taaislijmziekte en de ziekte van Alzheimer. *Hoofdstuk 5* beschrijft een nieuwe methode om experimentele gegevens over het vouwingsproces te verkrijgen. Twee spinlabels werden op verschillende plekken van het eiwit flavodoxine geplaatst. Met *double electron-electron resonance* (DEER) hebben we de afstand gemeten tussen de spinlabels op flavodoxine in verschillende concentraties denaturant. De met DEER verkregen afstandsverdelingen laten zien dat de lokale structuur in het ontvouwende eiwit kan worden gemeten en levert bewijs voor een vouwingsintermediair dat lokaal compacter is dan het eiwit in de native conformatie. We tonen aan dat we de ontvouwing van flavodoxine met DEER kunnen volgen en veranderingen in de lokale structuur kunnen meten die samengaan met ontvouwing.

CURRICULUM VITAE

Martin van Son was born on 9 January 1982 in Rotterdam, the Netherlands. After attending the Erasmiaans Gymnasium in Rotterdam, he studied chemistry at Leiden University. He completed research projects in coordination chemistry, solid-state chemistry, biophysical chemistry, and analytical chemistry, and graduated in August 2009. During his studies, he worked as a data processor at Fugro Aerial Mapping, which he continued afterwards. In May 2010, he started his doctorate research at the MoNOS group, Leiden Institute of Physics, under the supervision of dr. M. Huber and prof. dr. E.J.J. Groenen. His research was on protein interactions studied by electron-paramagnetic-resonance spectroscopy, the results of which are presented in this thesis.

As of August 2014, he is a lecturer in chemistry at the University of Applied Sciences in Leiden.

LIST OF PUBLICATIONS

H. Kooijman, M. van Son, S. Tanase, E. Bouwman, J. Reedijk, A.L. Spek: μ -oxo-bis{chloro[N-(2-methoxyethyl)-N,N-bis(pyridin-2-ylmethyl)amine-kappa (4)-N,N',N'',O]iron(III)}bis(trifluoromethanesulfonate) acetonitrile disolvate. *Acta Crystallographica Section E-Structure Reports Online* **61** (2005) M1042-M1044.

S. Tanase, M. van Son, G.A. van Albada, R. de Gelder, E. Bouwman, J. Reedijk: Self-assembly of extended structures through non-coordination intermolecular forces: Synthesis, crystal structures, and properties of metal complexes with 5-methyl-2-pyrazinecarboxylate. *Polyhedron* **25** (2006) 2967-2975.

G.J. Janssen, E. Daviso, M. van Son, H.J.M. de Groot, A. Alia, J. Matysik: Observation of the solid-state photo-CIDNP effect in entire cells of cyanobacteria *synechocystis*. *Photosynthesis Research* **104** (2010) 275-282.

M.H. Shabestari, M. van Son, A. Moretto, M. Crisma, C. Toniolo, M. Huber: Conformation and EPR characterization of rigid, 3(10)-helical peptides with TOAC spin labels: Models for Short Distances. *Biopolymers* **102** (2014) 244-251.

M. van Son, T.T. Zheng, P. Kumar, D. Valdink, J. Raap, A. Kros, M. Huber: Towards artificial membrane fusion: EK-peptides, the coiled-coil zipper. *Biophysical Journal* **106** (2014) 506A.

M. van Son, S. Lindhoud, C.P.M. van Mierlo, M. Huber: Equilibrium unfolding of flavodoxin from double electron-electron resonance distance constraints. *To be published*.

M. van Son, J. Schilder, P. Gast, A. Blok, M. Ubbink, M. Huber: The complex of cytochrome c with cytochrome c peroxidase studied by spin-label, multi-frequency electron paramagnetic resonance. *To be published*.

M. van Son, T.T. Zheng, P. Kumar, D. Valdink, J. Raap, A. Kros, M. Huber: Heterodimer formation of membrane fusion E/K-peptides studied by continuous-wave EPR. *To be published*.

ACKNOWLEDGEMENTS

Many people have contributed to the work that is presented in this booklet. I gladly mention them here.

I am most grateful to my doctoral supervisors, Martina Huber and Edgar Groenen, who allowed me to work and learn in the MoNOS group. They have taught me much about science, writing, and presenting. I carry their valuable lessons with me, whichever paths I shall tread in the future.

I wish to express my gratitude to the graduate students in the MoNOS group during the years that I was there: Maryam Hashemi Shabestari, Pravin Kumar, Faezeh Nami, and Gabriele Panarelli. I appreciated the experimental work we jointly performed, our discussions about EPR, and the laughter we shared. I was very fortunate that Silvia Sottini and Mykhailo Azarkh were working as postdocs in the group. Many times I knocked on their doors to ask them questions about EPR and other subjects. They were always prepared to share their knowledge with me. Big thanks to Matthijs van der Wild, who completed his bachelor's project in the MoNOS group. Matthijs performed the larger part of the DEER measurements that are shown in Chapter 5. I thank Henriette van Leeuwen and everybody else who has contributed his or her bit to the MoNOS group.

In 2011, Jos Disselhorst, Jan Schmidt, Huib Blok, Bert Crama, and Peter Gast joined forces to develop a new insert for the W-band spectrometer in order to improve its performance. The actual design and manufacturing of the insert was done by Harmen van der Meer. In December 2012, when the first tests were done, it became clear that the newly built insert outperformed the 'old' Bruker insert in all aspects. All of the W-band spectra presented in Chapter 3 were recorded with this new insert. I have greatly benefited from the development that was achieved by these experts.

I am thankful to Alexander Kros, Jan Raap, Tingting Zheng, Martin Rabe and Dayenne Valdink for their collaboration in the work of Chapter 2. I thank Marcellus Ubbink for allowing me to use the biochemical facilities of the Protein Chemistry group and for his collaboration in the work of Chapter 3. The biochemical work was uncharted territory when I started it. Luckily, I was aided by Marcellus's students: Qamar Bashir, Bharat Somireddy Venkata, Sandra Scanu, Jia-Ying Guan, Yoshitaka Hiruma, Wei-Min Liu, Jesika Schilder, Monika Timmer, and Simon Skinner. Special thanks to Anneloes Blok, whose constant support eventually led to a satisfactory labelling degree of cytochrome *c*. I thank Claudio Toniolo for his collaboration in the work of Chapter 4. Carlo van Mierlo and Simon Lindhoud are acknowledged for their collaboration in the work of Chapter 5.

It was a privilege to have the support of several technical departments. Hans van Kuyk is greatly acknowledged for supplying the liquid helium and nitrogen that I needed to do measurements at low temperatures. Gert Koning installed a new water pump needed to cool the EPR equipment. Ruud Kuyvenhoven and Arno van Amersfoort supported me whenever I needed help with computers. Frans Folst and Tom Jansen, the glassblowers at the Leidse instrumentmakers School, helped me with customized quartz tubes on numerous occasions.

It has been a joy to work with so many people within the Leiden Institute of Physics and the Leiden Institute of Chemistry. I am privileged to have met people from a large variety of cultures and I feel blessed that many of them have become my friends.